Available online at www.sciencedirect.com

ScienceDirect

Geochimica et Cosmochimica Acta 184 (2016) 193–211

Geochimica et Cosmochimica Acta

www.elsevier.com/locate/gca

Exploring the structural controls on helium, nitrogen and carbon isotope signatures in hydrothermal fluids along an intra-arc fault system

Daniele Tardani [a,b,*], Martin Reich [a,b], Emilie Roulleau [a,b], Naoto Takahata [c], Yuji Sano [c], Pamela Pérez-Flores [b,d], Pablo Sánchez-Alfaro [a,b], José Cembrano [b,d], Gloria Arancibia [b,d]

[a] Department of Geology, FCFM, Universidad de Chile, 8370450 Santiago, Chile
[b] Andean Geothermal Center of Excellence (CEGA), FCFM, Universidad de Chile, 8370450 Santiago, Chile
[c] AORI, Atmosphere and Ocean Research Institute, University of Tokyo, Kashiwa, Chiba 277-8564, Japan
[d] Department of Structural and Geotechnical Engineering, Pontificia Universidad Católica de Chile, 7820436 Santiago, Chile

Received 30 November 2015; accepted in revised form 18 April 2016; available online 26 April 2016

Abstract

There is a general agreement that fault-fracture meshes exert a primary control on fluid flow in both volcanic/magmatic and geothermal/hydrothermal systems. For example, in geothermal systems and epithermal gold deposits, optimally oriented faults and fractures play a key role in promoting fluid flow through high vertical permeability pathways. In the Southern Volcanic Zone (SVZ) of the Chilean Andes, both volcanism and hydrothermal activity are strongly controlled by the Liquiñe-Ofqui Fault System (LOFS), an intra-arc, strike-slip fault, and by the Arc-oblique Long-lived Basement Fault System (ALFS), a set of transpressive NW-striking faults. However, the role that principal and subsidiary fault systems exert on magma degassing, hydrothermal fluid flow and fluid compositions remains poorly constrained. In this study we report new helium, carbon and nitrogen isotope data ($^3He/^4He$, $\delta^{13}C–CO_2$ and $\delta^{15}N$) of a suite of fumarole and hot spring gas samples from 23 volcanic/geothermal localities that are spatially associated with either the LOFS or the ALFS in the central part of the SVZ. The dataset is characterized by a wide range of $^3He/^4He$ ratios (3.39 Ra to 7.53 Ra, where $Ra = (^3He/^4He)_{air}$), $\delta^{13}C–CO_2$ values (−7.44‰ to −49.41‰) and $\delta^{15}N$ values (0.02‰ to 4.93‰). The regional variations in $^3He/^4He$, $\delta^{13}C–CO_2$ and $\delta^{15}N$ values are remarkably consistent with those reported for $^{87}Sr/^{86}Sr$ in lavas along the studied segment, which are strongly controlled by the regional spatial distribution of faults. Two fumaroles gas samples associated with the northern "horsetail" transtensional termination of the LOFS are the only datapoints showing uncontaminated MORB-like $^3He/^4He$ signatures. In contrast, the dominant mechanism controlling helium isotope ratios of hydrothermal systems towards the south appears to be the mixing between mantle-derived helium and a radiogenic component derived from, e.g., magmatic assimilation of ^4He-rich country rocks or contamination during the passage of the fluids through the upper crust. The degree of ^4He contamination is strictly related with the faults controlling the occurrence of volcanic and geothermal systems, with the most contaminated values associated with NW-striking structures. This is confirmed by $\delta^{15}N$ values that show increased mixing with crustal sediments and meteoric waters along NW faults (AFLS), while $\delta^{13}C–CO_2$ data are indicative of cooling and mixing driving calcite precipitation due to increased residence times along such structures. Our results show that the structural setting of the region exerts a fist-order control on hydrothermal fluid composition by conditioning residence times of magmas

* Corresponding author at: Department of Geology, FCFM, Universidad de Chile, 8370450 Santiago, Chile.
E-mail address: daniele.tardani@ing.uchile.cl (D. Tardani).

http://dx.doi.org/10.1016/j.gca.2016.04.031

and thus promoting cooling/mixing of magmatic vapor, and therefore, must be taken into consideration for further geochemical interpretations.

Keywords: Helium isotopes; Nitrogen and carbon isotopes; Southern Volcanic Zone; Hydrothermal systems; Liquiñe-Ofqui Fault System

1. INTRODUCTION

In arc settings, helium isotopes have been successfully used, coupled with stable isotopes of carbon and nitrogen data, to constrain mantle heterogeneities and mechanisms of volatile recycling (Sano and Marty, 1995; Sano and Williams, 1996; Fischer et al., 1998, 2002; Sano et al., 2001). Subduction zones represent one of the preferential escape routes for primordial ^{3}He from the mantle, and previous studies have emphasized the role of the mantle wedge in dominating the helium budget in the great majority of cases (Hilton et al., 2002). Furthermore, it has been shown that participation of other contributors to the arc volatile inventory – i.e., the subducting slab and/or arc crust – can be traced using the isotopic composition of noble gases such as ^{3}He/^{4}He ratios and stable isotopes of carbon and nitrogen (Sano and Marty, 1995; Sano and Williams, 1996; Fischer et al., 1998, 2002; Sano et al., 2001). Such studies have proved critical to constrain the relative mantle vs. subducted sediment contributions on the isotopic signature of hydrothermal fluids, as well as the degree of contamination by upper crustal rocks. Despite these significant advances, very few studies have focused on deconvolving the regional scale structural and tectonic controls affecting the composition of deep-seated fluids during the separation from the magmatic source and the passage through the crust (Kennedy et al., 1997; Kennedy and van Soest, 2005; Karlstrom et al., 2013). In particular, the local scale control of interconnected faults and associated fractures (fault-fracture meshes; Sibson, 1996) on fluid flow in geothermal and hydrothermal systems has been largely studied over the past twenty years (Sibson, 1994, 1996; Manning and Ingebritsen, 1999; Sibson and Rowland, 2003; Fairley and Hinds, 2004; Micklethwaite and Cox, 2004; Rowland and Sibson, 2004; Blenkinsop, 2008; Graf and Therrien, 2009; Cox, 2010; Faulkner et al., 2010; Gudmundsson et al., 2010; Micklethwaite et al., 2010; Rowland and Simmons, 2012). These studies have improved our understanding about the structural factors controlling fluid flow, and have provided crucial information to refine conceptual models of the local fault-fracture hydraulic architecture in geothermal and hydrothermal systems.

The goal of this study is to unravel the regional scale structural controls on the isotopic composition of subduction-related magmatic gas, from its source to their pathway toward the surface. Our aim is to assess the nature of the link among fault-fracture meshes, magmatic degassing, crustal assimilation and fluid mixing processes taking place in the upper crust, that affect the composition of hydrothermal fluids discharged along principal and subsidiary structures of a regional scale, intra-arc strike slip fault. Considering the fact that tectonic activity defines the nature, geometry and kinematics of fault-fracture networks, a better understanding of the structural pattern and its link with the chemical evolution of fluids may give significant insights into the processes governing the dynamics of hydrothermal systems associated with such large-scale crustal structures.

The Andean Cordillera of Central-Southern Chile is a perfect natural laboratory to test this hypothesis. In this region, the relationship between tectonics and volcanism is the result of interaction between the crustal structures of the basement and the ongoing regional stress field (Pritchard et al., 2013). As pointed out by several studies, magmatism and volcanism, as well as geothermal activity in the region are spatially associated with tectonic features (Hildreth and Moorbath, 1988; López-Escobar et al., 1995; Hauser, 1997; Pérez, 1999; Sepúlveda et al., 2004; Lara et al., 2006; Cembrano and Lara, 2009; Alam et al., 2010; Lahsen et al., 2010; Sánchez et al., 2013). In particular, in the Southern Volcanic Zone (SVZ) between 37° and 46°S, the volcanic and geothermal activity is partially controlled by the ~1000 km long, NNE-striking intra-arc dextral strike-slip Liquiñe-Ofqui Fault System (LOFS), and by the NW-SE Arc-oblique Long-lived Basement Fault System (ALFS). Many geothermal surface manifestations and shallow fumarolic emissions are spatially related to stratovolcanoes and fault segments associated with both fault systems (Fig. 1).

Previous geochemical surveys conducted in this region have recognized a wide range of ^{3}He/^{4}He ratios in volcanic/geothermal fluids, suggesting mixing between mantle helium and the radiogenic helium sourced from country rocks (Hilton et al., 1993; Ray et al., 2009; Dobson et al., 2013). However, these studies have focused either on orogen-scale controls on noble gas compositions, or have addressed the local structural controls in individual geothermal systems (Sepúlveda et al., 2007; Agusto et al., 2013). In this study we present a comprehensive dataset of helium, nitrogen and carbon isotope analyses from a suite of about 20 volcanic fumaroles and thermal springs between the 37° and 41°S. The gas samples were collected from fumaroles in active volcanic systems and thermal springs that are closely spatially associated with both the LOFS and the ALFS. Based on new and unpublished mapped structures and as a up-to-date structural background in the region (Potent, 2003; Melnick et al., 2006; Lara et al., 2006; Cembrano and Lara, 2009; Pérez-Flores et al., 2014), we highlight the role of LOFS and ALFS on fluid circulation and provide a new interpretation that explains the spatial variations of helium, nitrogen and carbon isotopes in thermal fluids in the Central Southern Volcanic Zone of Chile.

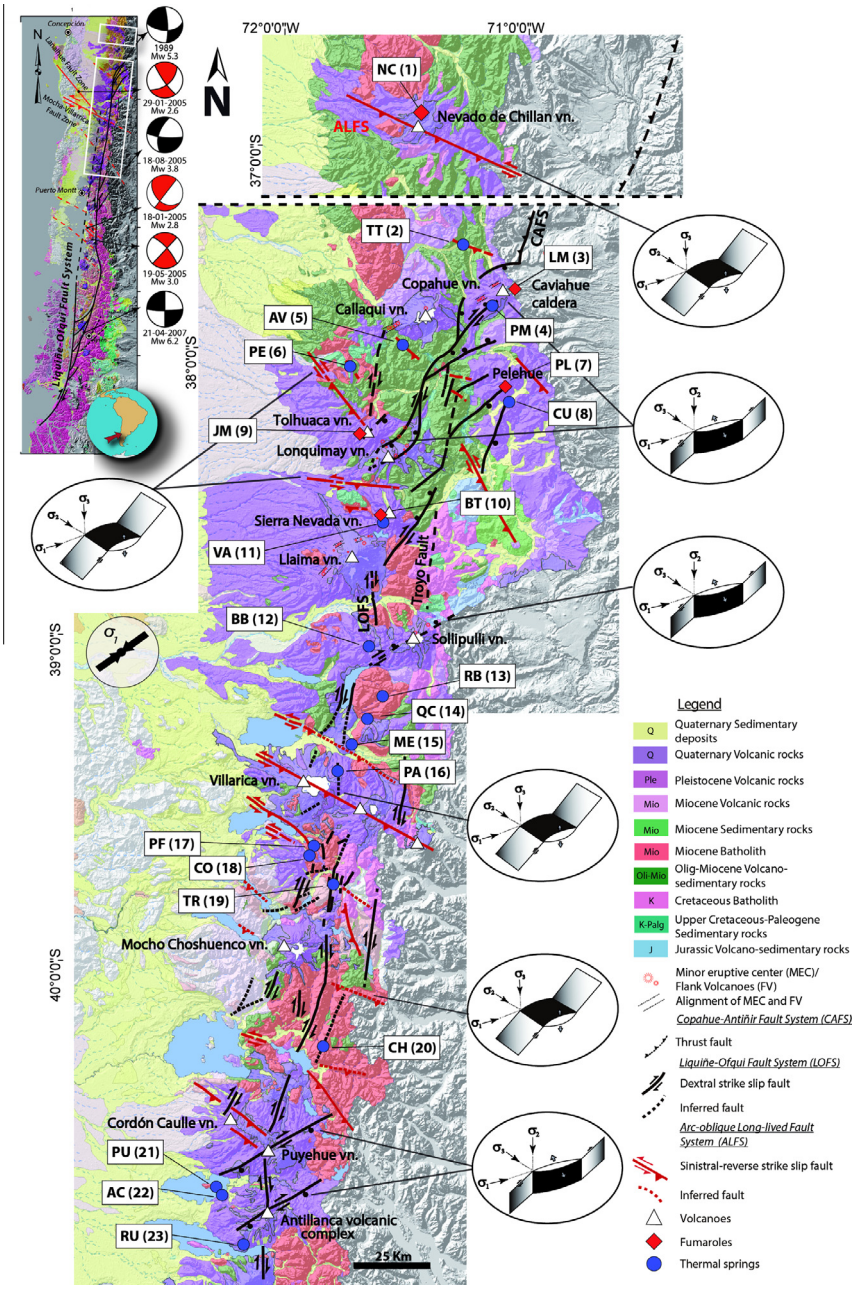

Fig. 1. Geologic and structural map of the central part the Southern Volcanic Zone (SVZ) in southern Chile. Solid and dashed lines represent main and secondary faults from Potent (2003), Melnick et al. (2006), Lara et al. (2006), Cembrano and Lara (2009), Sánchez et al. (2013) and Pérez-Flores et al. (2014). Blue circles and red diamonds represent the location of thermal springs and fumaroles samples, respectively. White triangles represent the main stratovolcanoes of the region. Sigma 1 (σ1) represent the maximum regional stress field. CAFS: Copahue-Antiñir Fault System, LOFS: Liquiñe-Ofqui Fault System, ALFS: Arc-oblique Long-lived Fault System. Stress fields for the distinct fault segments are modified from Sánchez et al. (2013) and Pérez-Flores et al. (2014). (For interpretation of the references to colour in this figure legend, the reader is referred to the web version of this article.)

2. GEOLOGICAL AND STRUCTURAL SETTING

The Southern Volcanic Zone (SVZ) of south-central Chile lies between 33°S and 46°S (Fig. 1). Along with the Central Volcanic Zone (CVZ, 14–28°S) and the Austral Volcanic Zone (AVZ, 49–55°S), it constitutes a three-segment active arc that comprises the Chilean Andes (Parada et al., 2007; Stern et al., 2007).

The Andean region examined in this study is about 450 km-long (37°–41°S), and forms part of the central and southern segments of the Southern Volcanic Zone (SVZ) (Fig. 1). In this region, the current geodynamic

setting is characterized by slightly oblique convergence between the Nazca and South American plates at a rate of ca. 7–9 cm/year that has prevailed for the last 20 Ma (Angermann et al., 1999; Somoza and Ghidella, 2005). The basement of the volcanic arc, in the northern portion of this segment at 39°S, is made up of extensive outcrops of the Meso–Cenozoic volcano–sedimentary rocks of the Cura Mallin and Cola de Zorro formations, which are locally intruded by Mio–Pliocene plutons (Charrier et al., 2002). South of 39°S, recent volcanic edifices are built directly onto Meso–Cenozoic plutonic rocks of the Patagonian Batholith. Crustal thickness underneath the volcanic arc decreases from 50 km at 33°S to 35 km at 46°S, with an accompanying decrease in the average altitude of the main cordillera, from 5000 m to less than 2000 m (Tassara and Yáñez, 2003).

The structural setting of the studied segment in Fig. 1 is dominated by the Liquiñe-Ofqui Fault System (LOFS), a NNE-striking, intra-arc transpressional dextral strike-slip fault system that extends between 37°S and 46°S, and associated with ENE-striking second-order intra-arc anisotropies (Cembrano et al., 1996, 2000; Folguera et al., 2002; Adriasola et al., 2006; Rosenau et al., 2006). The ENE-striking structures have been recognized as extensional fractures most likely formed under relatively low differential stress (Lavenu and Cembrano, 1999; Cembrano and Lara, 2009). Conversely, the arc oblique WNW-striking long-lived basement fault system (ALFS) is severely misoriented with respect to the prevailing stress field, and has been interpreted as crustal weaknesses associated with pre-Andean faults reactivated as sinistral-reverse strike–slip faults during the development of the arc (Cembrano and Moreno, 1994; López-Escobar et al., 1995; Lara et al., 2006; Melnick et al., 2006; Rosenau et al., 2006; Glodny et al., 2008; Lange et al., 2008).

The volcanism in the segment is represented by stratovolcanoes and monogenetic cones, many of which are spatially associated with the LOFS or ALFS. Their composition is mainly basaltic-andesitic with minor dacitic-rhyolitic occurrences. The stratovolcanoes and/or monogenetic cones exhibit mostly primitive magmatic signatures, and are related to secondary structures forming NE-trending volcanic alignments which are directly related to the current dextral transpressional tectonic regime (Lara et al., 2006; Cembrano and Lara, 2009). In contrast, the volcanic activity spatially related to the ALFS comprises WNW-trending volcanic alignments, where mostly stratovolcanoes occur. These include a wide range of compositions, with some centers having erupted only rhyolitic products in historical times. Because of their misorientation with respect to the prevailing stress field, the WNW-striking faults require supralithostatic magmatic pressures to become active (see Lara et al., 2004, 2006; Cembrano and Lara, 2009).

The northern segment of the LOFS (37.5–39°S) is characterized by transtensional deformation and shows an accommodation zone individuated by fault splays and graben formation. At 37.5°S, the interaction of the Liquiñe-Ofqui fault and the Copahue-Antiñir fault results in a NE-striking transitional zone (Melnick et al., 2006). At 38°S, the N–S to NNE-striking LOFS bends eastward and decomposes into a series of NE-striking extensional and transtensional fault splays that form an arrangement characterized by a "horsetail"-like geometry (Potent and Reuther, 2001; Rosenau et al., 2006). These types of structures have long been recognized to play a key role as host structures and high-permeability flow paths for geothermal systems and hydrothermal mineralization (Sibson, 1994, 1996; Rowland and Sibson, 2004; Rowland and Simmons, 2012).

3. SAMPLING AND ANALYTICAL TECHNIQUES

Gas and water samples were collected from fumaroles in active volcanic systems, bubbling hot springs and thermal water springs. Fumarole gases were sampled using a titanium tube, inserted into the fumarole or vent, and connected to a condenser and a water separator, to force water condensation. The dry gas obtained was collected in pre-evacuated alkaline glass containers with vacuum valves at both ends. Water and bubbling gas from hot springs were sampled in double valve, pre-evacuated alkaline glass containers, using pure silicone tubes connected to an inverted funnel and a manual pump. Dissolved gases from thermal water samples were extracted using a glass bottle under vacuum in the extraction line. Both methods for volcanic gases and water spring/bubbling gases are exhaustively described in Sano and Fischer (2013).

The $^{3}He/^{4}He$ ratios were measured using a noble gas mass spectrometer (Helix-SFT) at the Atmosphere and Ocean Research Institute (AORI), University of Tokyo, Japan. The $^{4}He/^{20}Ne$ ratios were measured using a quadrupole mass spectrometer. Helium and neon were separated using a cryogenic trap operated at 40 K (see Sano and Wakita, 1988). The measured $^{3}He/^{4}He$ ratios were calibrated against atmospheric helium. Experimental errors of $^{4}He/^{20}Ne$ and $^{3}He/^{4}He$ ratios are about 0.5% and 1% at 1σ, respectively (Sano et al., 2008). Assuming that the Air Saturated Water (ASW) neon content is significantly higher than in mantle and crustal gases, the R/Ra can be corrected for the presence of atmospheric helium using the $^{4}He/^{20}Ne$ ratio of the sample (Craig et al., 1978). The error calculation for air corrected helium was performed using the procedure described in Sano et al. (2006).

The $\delta^{13}C$ and $\delta^{15}N$ values of gas samples were measured using a conventional gas source mass spectrometer (IsoPrim100, Isoprime Ltd.) at AORI. All values were corrected for blanks that represent 0.2% of the measurement contribution (Barry et al., 2012). The error of the delta values is the propagated error of the isotopic measurement of N and C in the sample, the standard and the blank, assumed at 1σ. The carbon isotopic composition was measured in CO_2 and CH_4 gaseous component and is expressed in delta notation as:

$$\delta^{13}C = \left([^{13}C/^{12}C]_{sample} / [^{13}C/^{12}C]_{STD} - 1 \right) \times 1000$$

The nitrogen isotopic composition is given by:

$$\delta^{15}N = \left([^{15}N/^{14}N]_{sample} / [^{15}N/^{14}N]_{air} - 1 \right) \times 1000$$

The chemical composition (He, CH_4, N_2, O_2, Ar, H_2S and CO_2) of sampled gases was measured using a quadrupole mass spectrometer at AORI, by comparing peak heights of the sample with those of standard gases. Experimental errors were estimated to be about ±10% by repeated measurements of standard samples. The blank for each component was significantly lower compared to the sample signals.

4. RESULTS

Tables 1 and 2 present the chemical composition and isotopic data (R/Ra, $^4He/^{20}Ne$, air-corrected $^3He/^4He$ (Rc/Ra) ratios, $\delta^{15}N$, $\delta^{15}N_C$, $\delta^{13}C–CO_2$ and $\delta^{13}C–CH_4$ values) of gas samples from 23 volcanic/geothermal localities, including 5 fumaroles, 7 bubbling gas and 11 hot springs (water-dissolved gas). In the tables, samples are sorted in latitudinal order and labeled with a sample name and with an ID label, from 1 to 23, from north to south. Furthermore, and for the sake of simplicity, we will refer to samples as fumarole gas and hot spring gas samples. Fig. 1 shows sample locations and their association with the main structural features of the LOFS and ALFS.

4.1. Gas composition

All five fumarole gas samples are dominated by CO_2, representing at least the 80% of the total gas in each sample. For the hot spring gas, the samples AV (5), PE (6), VA (11), QC (14), PA (16), CO (18), TR (19), CH (20), AC (22) and RU (23) are dominated by N_2, while the others are dominated by CO_2, with the exception of the CH_4-dominated TT (2) sample. Methane was also detected in all other samples, with six of them showing concentrations that are higher than 1%. The reduced sulfur compound H_2S was detected in seven samples. The five fumarole gas samples present the highest H_2S concentrations, while PE (6) and PM (4) are the only two hot spring gas where H_2S concentrations are detectable.

The majority of fumarole and hot spring gas samples have O_2 contents lower than 5%, with the exception of four samples (AV (5), RB (13), PU (21) and RU (23)). Three of these samples (RB (13), PU (21) and RU (23)) have N_2/O_2 close to the air ratio, of 3.73, suggesting a significant atmospheric contamination. In contrast, the helium isotope composition was not strongly affected by atmospheric helium in these three samples, suggesting that the contamination has probably happened during analysis. The $^4He/^{20}Ne$ ratios are 1.57, 1.37 and 4.20 respectively, at least four times higher than the air ratio (0.33).

In Fig. 2, the inert (He and Ar) and nearly inert (N_2) gas compositions are plotted in a ternary diagram, and used as a source indicator for the origin of volatile components (after Giggenbach and Goguel, 1989; Giggenbach and Poreda, 1993). The N_2/Ar ratio of the samples varies between 38.73 and 544.73. All samples, with the exception of sample PL (7), roughly fit a mixing trend between arc-derived fluids (“Arc-type sediments”) and a second end-member comprised between the atmospheric value (“Air”) and the Air-Saturated Water value (“ASW”). The presence of atmospheric gases in the mixture is visible in Fig. 2, and is consistent with previously published data by Ray et al. (2009) for the region. Fumarolic outlier gas sample PL (7), instead, shows a mantle-fluid affinity with atmospheric (air) contribution.

The $CO_2/^3He$ ratios were calculated from CO_2/He and $^3He/^4He$ ratios for each sample. The $CO_2/^3He$ ratios for water-dissolved gases and bubbling gases cover an exceptionally wide range between 116.01×10^9 (CU (8)) and 5.08×10^5 (AV (5)) (Fig. 3). More than half of the samples show $CO_2/^3He$ ratios lower than MORB ($2.0 \pm 1.0 \times 10^9$; Marty and Jambon, 1987) and global arc-like values ($1.5 \pm 1.1 \times 10^{10}$; e.g. Sano and Williams, 1996), in agreement with previous data for the region (e.g., Ray et al., 2009). All fumarolic gas samples range from 17.78×10^9 (NC (1)) to 1.56×10^9 (PL (7)), and are included in the global arc average field (with the exception of sample PL (7) plotting in the MORB field). The hot spring samples PM (4) (57.83×10^9) and CU (8) (116.01×10^9) are the only ones exceeding the global arc average value.

4.2. He, N and C isotope composition

The helium, carbon and nitrogen isotope compositions of thermal manifestations along the SVZ of south-central Chile are highly variable and are not directly correlated with their distance from stratovolcanoes. In contrast, as shown in Fig. 4, the helium, carbon and nitrogen isotopic ratios show remarkably similar latitudinal tendencies, analogous to the trend of $^{87}Sr/^{86}Sr$ ratios in lavas of principal stratovolcanoes in the segment. Along-arc variations in strontium isotope composition of volcanic rocks are indicative of variable degrees of crustal contamination, most likely due to intracrustal assimilation (Hildreth and Moorbath, 1988; Hickey-Vargas et al., 1989), and/or source region contamination by subducted continental components (Stern, 1991; Kay et al., 2005). The observed variations in helium, carbon and nitrogen isotopes along the studied segment do not seem to correlate with crustal thickness (Moho depth is represented by the red line in Fig. 4), but rather with the regional distribution of NE- and NW-striking faults (Figs. 1 and 4). This observation is in agreement with the fact that these structures play a first order control on the migration and storage of magmas along the SVZ, as studies by Lara et al. (2006) and Cembrano and Lara (2009) have reported.

4.2.1. *$^3He/^4He$ ratios*

The air-corrected $^3He/^4He$ ratios (Rc/Ra), given as multiples of the present-day atmospheric ratio ($Ra = 1.382 \times 10^{-6}$; Sano et al., 2013; Mabry et al., 2013), range from 3.68 Ra to 7.67 Ra (Table 2). The northern part of the studied segment (~37.5–38.5°S) shows the widest range of Rc/Ra values, (Fig. 4). The highest values were found in two fumarolic gas samples (LM (3) and PL (7)) associated with the transtensional “horsetail” structure in the northern part of the LOFS. High ratios were also found, from north to south, in two bubbling gas samples (PM (4) and CU (8)), in a fumarolic gas sample from the Tolhuaca volcano (JM (9)), and in the bubbling gas sample

Table 1
Chemical composition of SVZ fumarole, bubbling gas and water-dissolved gas samples.

Sample id	Sample name	Location	Latitude S	Longitude O	Date	Sample type	Temperature °C	He ppm	CH_4	N_2	O_2	Ar	H_2S	CO_2	N_2/He × 10^5	N_2/O_2	N_2/Ar	He/Ar
1	NC	Nevado de Chillan Vn.	36° 54.317′	71° 24.085′	Nov-13	F	91.0	8.62	0.09%	11.68%	2.25%	0.14%	12.86%	72.99%	0.14	5.19	82.41	0.01
2	TT	Trapa Trapa	37° 41.971′	71° 17.098′	Jan-15	WD	45.0	89.10	57.10%	42.03%	n.d.	0.56%	n.d.	0.33%	0.05	–	75.44	0.02
3	LM	Las Maquinas (Copahue Vn.)	37° 50.036′	71° 5.055′	Jan-14	F	93.0	10.85	2.80%	2.70%	0.03%	0.00%	0.44%	94.03%	0.02	105.24	544.73	0.22
4	PM	Pucon Mahuida	37° 53.811′	71° 10.536′	Nov-13	WD	47.0	1.99	0.01%	0.67%	0.04%	0.01%	0.01%	99.27%	0.03	16.00	89.79	0.03
5	AV	Termas del Avellano	37° 59.378′	71° 31.938′	Jan-15	BG	65.3	240.60	0.16%	90.42%	8.43%	0.89%	n.d.	0.08%	0.04	10.73	102.17	0.03
6	PE	Termas de Pemehue	38° 4.579′	71° 42.082′	Jan-14	WD	38.5	88.80	1.38%	73.24%	0.42%	0.32%	0.46%	24.17%	0.08	174.01	231.40	0.03
7	PL	Pelehue	38° 7.367′	71° 3.486′	Nov-13	F	93.4	53.52	0.05%	4.11%	0.08%	0.05%	7.71%	87.98%	0.01	51.80	90.58	0.12
8	CU	Termas de Coyuco	38° 11.422′	71° 2.182′	Jan-15	WD	36.0	1.02	0.18%	2.40%	n.d.	0.06%	n.d.	97.35%	0.24	–	38.73	0.00
9	JM	Jaime Muro (Tolhuaca Vn.)	38° 17.409′	71° 40.057′	Jan-14	F	92.0	8.17	0.03%	3.60%	0.04%	0.01%	1.10%	95.22%	0.04	89.41	430.38	0.10
10	BT	Baños del Toro (Sierra Nevada Vn.)	38° 34.487′	71° 36.951′	Jan-14	F	87.0	15.40	0.02%	8.74%	0.02%	0.05%	4.74%	86.42%	0.06	560.17	180.00	0.03
11	VA	Agua de la Vaca	38° 34.809′	71° 37.685′	Feb-15	BG	35.0	29.02	0.08%	93.65%	3.99%	1.32%	n.d.	0.96%	0.32	23.47	70.96	0.00
12	BB	Termas de Balboa	38° 57.628′	71° 42.627′	Nov-14	BG	45.0	6.02	0.03%	32.24%	4.84%	0.44%	n.d.	62.54%	0.54	6.67	73.41	0.00
13	RB	Termas de Rio Blanco	39° 06.468′	71° 36.820′	Nov-14	WD	47.0	96.08	0.08%	20.10%	5.22%	0.46%	n.d.	74.24%	0.02	3.85	43.80	0.02
14	QC	Termas Quimey-Có	39° 13.168′	71° 41.750′	Nov-14	BG	45.0	37.80	0.09%	95.05%	3.54%	1.27%	n.d.	0.04%	0.20	26.81	74.98	0.00
15	ME	Parque Termal Menetùe	39° 19.527′	71° 43.113′	Nov-14	WD	42.0	261.33	0.05%	44.11%	1.39%	1.12%	n.d.	53.45%	0.02	31.74	39.40	0.02
16	PA	Termas de Palguin	39° 25.343′	71° 47.145′	Nov-14	BG	50.0	51.10	8.47%	89.89%	0.23%	1.22%	n.d.	0.19%	0.15	398.94	73.69	0.01
17	PF	Eco Termas Pellaifa	39° 38.030′	71° 55.208′	Nov-14	WD	50.0	48.29	0.01%	9.96%	1.11%	0.25%	n.d.	88.57%	0.02	8.95	40.42	0.02
18	CO	Termas de Coñaripe	39° 38.097′	71° 55.437′	Nov-14	WD	74.6	36.09	2.16%	66.82%	1.47%	1.37%	n.d.	28.42%	0.19	45.35	48.68	0.00
19	TR	Termas de Trafipan	39° 44.175′	71° 51.651′	Nov-14	WD	37.2	45.09	0.09%	96.74%	n.d.	1.44%	n.d.	1.78%	0.21	-	67.23	0.00
20	CH	Termas de Chihuio	40° 11.407′	71° 55.954′	Jan-15	WD	82.5	49.28	0.09%	96.23%	1.64%	1.70%	n.d.	0.34%	0.20	58.51	56.72	0.00
21	PU	Termas de Puyehue	40° 42.645′	72° 19.403′	Jan-15	WD	60.0	21.92	0.12%	78.32%	14.99%	1.37%	n.d.	5.21%	0.03	5.22	56.98	0.00
22	AC	Termas de Aguas Calientes	40° 43.918′	72° 18.357′	Jan-15	BG	66.0	166.60	0.13%	96.62%	1.37%	1.43%	n.d.	0.43%	0.05	70.30	67.44	0.01
23	RU	Termas de Rupanco	40° 51.386′	72° 13.459′	Jan-15	BG	80.0	11.75	1.28%	79.10%	18.65%	0.90%	n.d.	0.07%	0.67	4.24	87.67	0.00

Note: F, fumarole gas; WD, water-dissolved gas; BG, bubbling pool gas.

Table 2
Isotopic composition of SVZ fumarole, bubbling gas and water-dissolved gas samples.

Sample id	Sample name	Location	$^4He/^{20}Ne$	$^{20}Ne/^4He$	$^3He/^4He$[a] Ra	±	$^3He/^4He$[b] Rc/Ra	±	$CO_2/^4He \times 10^4$	$CO_2/^3He \times 10^9$	$\delta^{15}N$	±	$\delta^{15}N_C$	±	$\delta^{13}C$ (CO_2)	±	$\delta^{13}C$ (CH_4)	±
1	NC	Nevado de Chillan Vn.	3.05	0.33	3.40	0.07	3.68	0.10	8.47	17.78	0.37	0.20	5.56	0.20	−9.30	0.14	n.a.	–
2	TT	Trapa Trapa	48.77	0.02	4.38	0.09	4.40	0.00	0.00	0.01	2.89	0.21	6.34	0.21	−25.52	0.27	−44.08	0.27
3	LM	Las Maquinas (Copahue Vn.)	67.55	0.01	7.48	0.15	7.52	0.01	8.67	8.27	4.93	0.20	6.16	0.20	−7.96	0.14	−34.38	0.14
4	PM	Pucon Mahuida	27.58	0.04	6.16	0.12	6.23	0.02	49.91	57.83	4.42	0.21	6.28	0.21	−11.87	0.14	n.a.	–
5	AV	Termas del Avellano	21.32	0.05	4.41	0.09	4.46	0.00	0.00	0.00	1.74	0.20	5.56	0.20	−20.40	0.30	n.a.	–
6	PE	Termas de Pemehue	55.52	0.02	4.69	0.10	4.71	0.01	0.27	0.41	3.35	0.20	6.64	0.20	−25.80	0.20	n.a.	–
7	PL	Pelehue	15.70	0.06	7.53	0.15	7.67	0.10	1.64	1.56	1.03	0.20	1.60	0.20	−7.44	0.14	n.a.	–
8	CU	Termas de Coyuco	2.24	0.45	5.89	0.13	6.69	0.10	95.62	116.01	n.a.	–	–	–	−7.75	0.27	n.a.	–
9	JM	Jaime Muro (Tolhuaca Vn.)	16.07	0.06	6.38	0.13	6.49	0.05	11.65	13.04	3.92	0.20	6.52	0.20	−9.75	0.14	n.a.	–
10	BT	Baños del Toro (Sierra Nevada Vn.)	51.34	0.02	4.59	0.09	4.61	0.01	5.61	8.73	2.69	0.20	6.40	0.20	−8.79	0.14	−31.44	1.10
11	VA	Agua de la Vaca	2.49	0.40	3.91	0.08	4.33	0.01	0.03	0.06	0.26	0.22	5.68	0.22	−13.72	0.27	n.a.	–
12	BB	Termas de Balboa	5.22	0.19	6.34	0.06	6.75	0.03	10.39	11.71	n.a.	–	–	–	−19.18	0.28	n.a.	–
13	RB	Termas de Rio Blanco	1.57	0.64	3.56	0.00	4.36	0.04	0.77	1.55	n.a.	–	–	–	−17.00	0.30	n.a.	–
14	QC	Termas Quimey-Có	2.66	0.38	4.67	0.05	5.27	0.03	0.00	0.00	0.02	0.20	–	–	−30.72	0.30	n.a.	–
15	ME	Parque Termal Menetùe	4.47	0.22	5.05	0.01	5.42	0.01	0.20	0.29	n.a.	–	–	–	−27.36	0.53	n.a.	–
16	PA	Termas de Palguin	4.17	0.24	3.58	0.07	3.79	0.00	0.00	0.01	0.10	0.20	–	–	−49.41	0.28	−66.70	0.28
17	PF	Eco Termas Pellaifa	1.28	0.78	3.39	0.04	4.38	0.06	1.83	3.86	n.a.	–	–	–	−23.89	0.36	n.a.	–
18	CO	Termas de Coñaripe	1.73	0.58	3.69	0.10	4.29	0.03	0.79	1.53	0.52	0.23	5.80	0.23	−20.05	0.28	n.a.	–
19	TR	Termas de Trafipan	2.70	0.37	4.43	0.09	4.89	0.02	0.04	0.06	0.24	0.23	5.44	0.23	−23.67	0.58	n.a.	–
20	CH	Termas de Chihuio	3.36	0.30	4.08	0.08	4.40	0.01	0.01	0.01	0.09	0.20	–	–	−23.04	0.36	n.a.	–
21	PU	Termas de Puyehue	1.37	0.73	4.89	0.11	6.07	0.17	0.24	0.34	n.a.	–	–	–	−22.64	0.30	n.a.	–
22	AC	Termas de Aguas Calientes	14.15	0.07	6.77	0.14	6.91	0.01	0.00	0.00	1.32	0.20	5.56	0.20	−20.49	0.27	n.a.	–
23	RU	Termas de Rupanco	4.20	0.24	6.52	0.13	6.97	0.04	0.01	0.01	n.a.	–	–	–	−14.70	0.27	n.a.	–

Note: $CO_2/^3He$ is calculated from CO_2/He and $^3He/^4He$ ratios. Error for $^4He/^{20}Ne$ is 5%.

[a] $^3He/^4He$ (Ra) ratios are calculated using $^3He/^4He$ of air (1.40×10^{-6} ccSTP/g).

[b] $^3He/^4He$ (Rc/Ra) is the denomination for corrected $^3He/^4He$ from $^4He/^{20}Ne$.

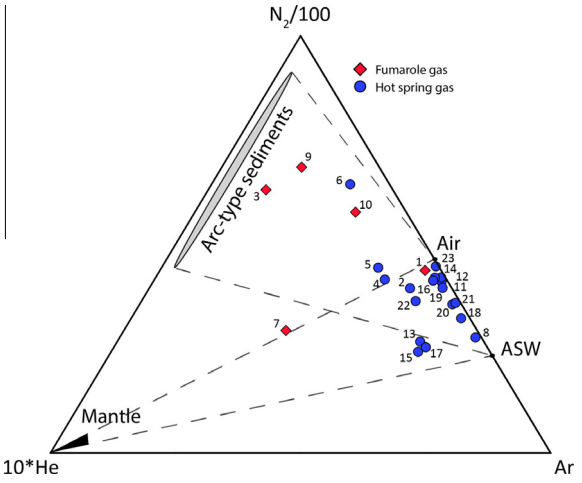

Fig. 2. Ternary plot of the relative N_2, He and Ar contents of SVZ fumaroles (red diamond) and hot spring (blue circles) gas samples. The end-member components, i.e., mantle, arc-type, air and Air Saturated Water (ASW) are shown for comparison. (For interpretation of the references to colour in this figure legend, the reader is referred to the web version of this article.)

BB (12), associated with the Sollipulli volcano. Rc/Ra values are also high in the southern part of the studied area, where three hot spring gas samples (PU (21), AC (22) and RU (23)), close to Puyehue-Cordon Caulle and Casablanca volcanoes, reach MORB-like values. Accordingly, lavas from stratovolcanoes associated with these high Rc/Ra fumaroles and thermal springs show lower strontium isotope ratios ($^{87}Sr/^{86}Sr$) reflecting a low degree of crustal contamination of these magmatic volatile sources (Fig. 4).

In contrast, the central part of the studied segment, (~38.5–40°S), as well as the northernmost limit at the Nevados de Chillán volcano (~37°S), show lower helium ratios and a narrower distribution of Rc/Ra values, ranging between 5.42 ± 0.01 Ra and $3.68 \pm 0{,}10$ Ra. The stratovolcanoes associated with these manifestations present higher values of $^{87}Sr/^{86}Sr$ ratio in lavas, indicating a higher crustal assimilation of the deep magmatic system.

4.2.2. Carbon isotopes ($\delta^{13}C$–CO_2)

The measured $\delta^{13}C$–CO_2 values range from -7.44 ± 0.14‰ to -49.41 ± 0.28‰ (Table 2; Fig. 4). Fumarolic gases have the higher values, ranging between -7.44 ± 0.14‰ and -9.75 ± 0.14‰. LM (3) and PL (4) samples, in particular, have MORB-like (-6.5 ± 2.2‰; e.g., Sano and Marty, 1995) and high temperature volcanic gas (-5.5 ± 2.2‰; e.g. Sano and Marty, 1995; Sano and Williams, 1996) signatures. Hot spring gas samples range between -11.87 ± 0.14‰ and -49.41 ± 0.28‰, except for one sample that has more affinity to a fumarolic gas-like signature (sample CU (8), -7.44 ± 0.14‰).

In agreement with Rc/Ra and $^{87}Sr/^{86}Sr$ trends, the stable isotopes of carbon ($\delta^{13}C$–CO_2) show a regional distribution where the highest (heaviest) values are restricted to the northernmost and southernmost parts of the studied segment. The central part of studied region shows lighter carbon signatures. The lightest value (−49.41‰) corresponds to the bubbling gas sample PA (16) and is coincident with a very low $CO_2/^3He$ value (6.1×10^6) and with the second lowest Rc/Ra value in the region (3.78 Ra).

4.2.3. Nitrogen isotopes ($\delta^{15}N$)

The $\delta^{15}N$ values range from 0.02 ± 0.20‰ to 4.93 ± 0.20‰, in agreement with subduction-zone signatures (−5‰ to +7‰; Fischer et al., 2002; Hilton et al., 2002). The highest $\delta^{15}N$ values occur in the northern part and the southernmost part of the studied region. The highest $\delta^{15}N$ values, in particular, were measured in the fumarole gas sample LM (3) and the bubbling gas sample PM (4), which are both associated with the Copahue volcano in the northernmost "horsetail" termination of the LOFS. In

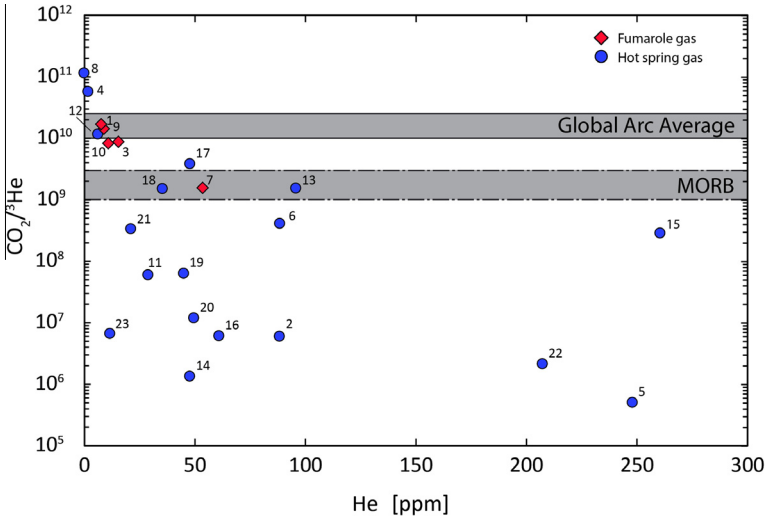

Fig. 3. $CO_2/^3He$ versus He concentration plot of SVZ fumaroles (red diamonds) and hot-spring (blue circles) gas samples. Global arc average ($1.5 \pm 1.1 \times 10^{10}$; e.g. Sano and Williams, 1996) and MORB ($2.0 \pm 1.0 \times 10^9$; e.g. Marty and Jambon, 1987) fields are shown. (For interpretation of the references to colour in this figure legend, the reader is referred to the web version of this article.)

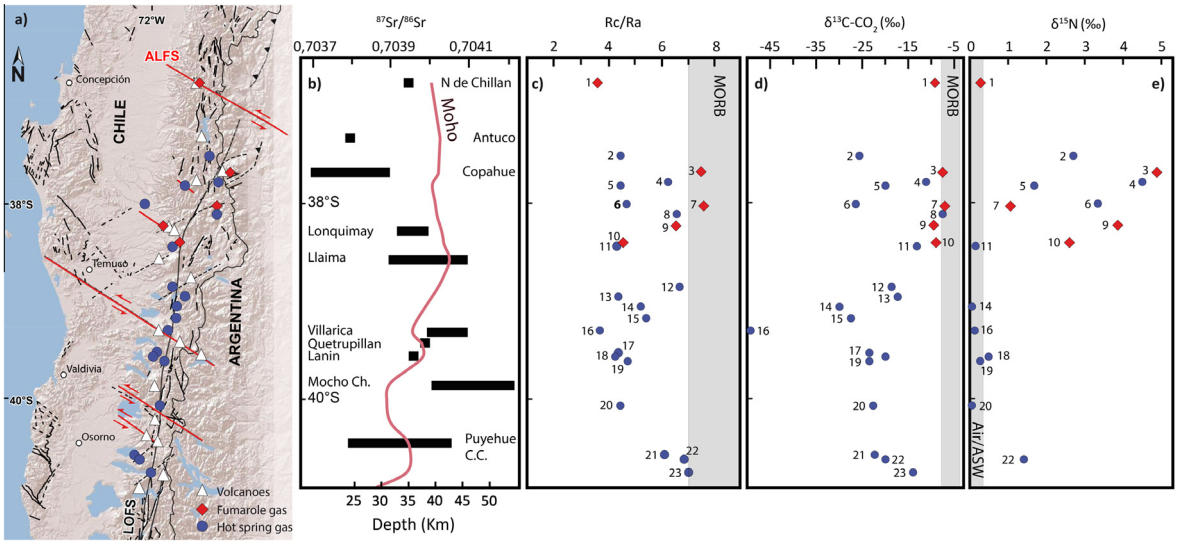

Fig. 4. (a) Digital elevation model of the central part of the Southern Volcanic Zone in southern Chile. White triangles represent main stratovolcanoes of the segment. Red diamonds and blue circles represent the location of fumarole and hot spring gas samples, respectively. Solid and dashed lines show simplified faults and lineations from Potent (2003), Lara et al. (2006), Cembrano and Lara (2009), Sánchez et al. (2013) and Pérez-Flores et al., 2014; (b) $^{87}Sr/^{86}Sr$ ratios of lavas from stratovolcanoes of SVZ. Data compiled from Deruelle et al. (1983), Davidson et al. (1987), Gerlach et al. (1988), McMillan et al. (1989), Hickey-Vargas et al. (1989) and Varekamp et al. (2006). The red line represents the depth of the MOHO from Tassara et al. (2006); (c) Latitudinal variation of corrected $^{3}He/^{4}He$ (Rc/Ra) ratios; (d) Latitudinal variation of $\delta^{13}C–CO_2$; (e) Latitudinal variation of $\delta^{15}N$. (For interpretation of the references to colour in this figure legend, the reader is referred to the web version of this article.)

contrast, all thermal springs in central part of the segment, between 38.5°S and 40°S (and the fumarole gas sample NC (1)) show $\delta^{15}N$ ratios near 0‰.

5. DISCUSSION

The isotope data of fumaroles and bubbling gas samples presented here show that fluids in the studied segment are characterized by a wide spectrum of Rc/Ra, $\delta^{15}N$, $\delta^{13}C–CO_2$ and $CO_2/^{3}He$ values. As shown in Fig. 4, the isotopic compositions are highly variable along the studied area and can be correlated with strontium isotope data in the region. In particular, the northern and southern parts of the studied region are characterized by more primitive helium (Rc/Ra), carbon ($\delta^{13}C–CO_2$) and nitrogen ($\delta^{15}N$) values (Fig. 4). This trend is reversed in the central part of the segment (~38.5–40°S), where Rc/Ra, $\delta^{13}C–CO_2$ and $\delta^{15}N$ values are lower and may be related to secondary processes taking place in the shallow crust.

In the following sections we discuss the possible fractionation processes affecting the helium, nitrogen and carbon isotopic signatures in the region. We evaluate the effects of crustal contamination and meteoric fluid mixing on magmatic volatile compositions during the migration towards the surface, and we explore the link between these processes and the structural/tectonic framework of the region (LOFS and ALFS).

5.1. Crustal assimilation and contamination

Crustal contamination can modify the $^{3}He/^{4}He$, $CO_2/^{3}He$ ratios and $\delta^{15}N$, $\delta^{13}C–CO_2$ values through the addition of radiogenic ^{4}He, N_2 and CO_2 from crustal rocks (Sano et al., 1998). In the SVZ, previous studies have pointed out that the main control on the measured $^{3}He/^{4}He$ values is related to a combination of near surface magmatic degassing and crustal contamination of degassed magmas (Hilton et al., 1993, 2002; Ray et al., 2009). However, the aforementioned studies did not address the potential effects of regional and/or local structures on crustal contamination and magmatic degassing. Therefore, the impacts of volcano-tectonic associations on R/Ra variability remain to be tested.

As shown in Fig. 5, the $^{3}He/^{4}He$ ratios (R/Ra) of analyzed samples in the studied area range between 3.40 Ra and 7.53 Ra. All the fumarole and hot springs gas samples are significantly higher than purely crustal values (~0.05 Ra; e.g. Morrison and Pine, 1955), indicating that the whole segment receives a significant contribution of mantle-derived helium. We calculate that at least 45% of helium in the gas phase is derived from the mantle, representing the baseline of the whole segment (Fig. 5). From Fig. 5, it is evident that well-defined data point clusters may be indicative of variations in the degree of crustal contamination, i.e., coinciding with the different structures that control the volcanic/geothermal manifestations in the region. For example, the two fumarole gas samples in Copahue (LM (3)) and Pelehue (PL (7)) show the highest R/Ra ratios (7.48 Ra and 7.53 Ra, respectively) and are the only samples fitting the MORB field (8 ± 1 Ra; after Farley and Neroda, 1998; Graham, 2002). These samples are characterized by very low degrees of crustal contamination (Fig. 5), and are associated with two fault splays located in the northernmost "horsetail" termination of

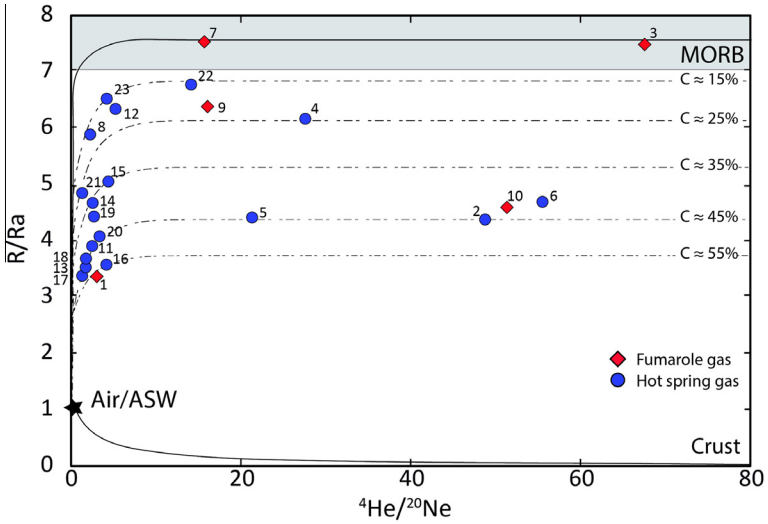

Fig. 5. R/Ra versus ^{4}He/^{20}Ne plot of SVZ fumaroles (red diamonds) and hot springs (blue circles) gas samples. The end-member MORB, crust, Air and Air-Saturated Water (ASW) are reported. Dashed lines represents the calculated mixing curves between crustal contamination degrees of 15%, 25%, 35%, 45% and 55%, and the Air/ASW endmember. (For interpretation of the references to colour in this figure legend, the reader is referred to the web version of this article.)

the LOFS (Fig. 1). In addition, two hot springs samples (PM (4) and CU (8)) that are associated with the aforementioned fumaroles samples also exhibit high ^{3}He/^{4}He values at 6.16 Ra and 5.89 Ra, respectively. Mixing models show additions of crustally derived He that range between 20% and 25% (Fig. 5).

The fumarole gas sample JM (9), the three bubbling gas BB (12), AC (22), RU (23) and the water-dissolved gas sample PU (21), also present high ^{3}He/^{4}He ratios (6.77 to 4.89 Ra, Table 2). Also, the fumarole gas sample at "Las Sopas", associated with Cordón-Caulle volcano, fit within the same range, with a ^{3}He/^{4}He ratio of 6 Ra (Sepúlveda et al., 2007). As shown in Fig. 5, these samples are characterized by ~15–25% of contamination with crustal helium. All these intermediate to high R/Ra emissions, as shown in Fig. 1, are associated with volcanoes that are controlled by NE-striking extensional faults (e.g., Sollipulli volcano), or by the intersection between NE- and NW-striking faults (Tolhuaca and Puyehue-Cordon Caulle volcanoes). The aforementioned analysis strongly suggests that R/Ra values in fumaroles and hot springs in the studied area are influenced by crustal contamination processes that are at least partially controlled by regional and/or local structures. In the next paragraphs we use δ^{15}N, δ^{13}C–CO_2 data and mixing models to provide further evidence to support this assumption.

In Fig. 6, the δ^{15}N is plotted with N_2/He (a) and N_2/Ar (b) ratios. Nitrogen contribution end members from sediments ($\delta^{15}N = +7‰$; $N_2/He = 1.05 \times 10^4$), MORB ($\delta^{15}N = -5‰$; $N_2/He = 1.5 \times 10^2$) and air/ASW ($\delta^{15}N = 0‰$ and $N_2/He = 1.49 \times 10^5$) are reported in Fig. 6a (from Sano et al., 1998; Ozima and Podosek, 2002; Fischer et al., 2002; Clor et al., 2005). The mixing curves are defined as:

$$\delta^{15}N_{obs} = A \times \delta^{15}N_{air} + M \times \delta^{15}N_{MORB} + S \times \delta^{15}N_{sed}$$

$$1/(N_2/He)_{obs} = A/(N_2/He)_{air} + M/(N_2/He)_{MORB} + S/(N_2/He)_{sed}$$

$$A + M + S = 1$$

where *obs*, *air*, *MORB* and *sed* refer to the observed values of air, MORB and sediments, respectively, while A, M and S are the fractions of air, MORB and sediments, respectively.

According to the literature, the N_2/He values for volcanic arc samples typically range between 1000 and 10,000, with lowest and highest values reported at 101 and 24,899, respectively (Giggenbach and Corrales, 1992; Giggenbach and Glover, 1992; Giggenbach and Poreda, 1993; Fischer et al., 2002; Clor et al., 2005). These values are significantly higher than those observed in MORBs (N_2/He ~ 150; Sano et al., 2001).

The percentage of sediments in the mixture for almost all the samples varies between 88% and 97%, in agreement with gas data from the Copahue volcano (Agusto et al., 2013). Sample PL (7) at Pelehue deviates the general trend, accordingly with the He-N_2-Ar diagram in Fig. 2, and shows a more pronounced MORB signature with only a 55% contribution from the sediments endmember. This signature is also confirmed by the corrected ^{3}He/^{4}He ratio with the highest value in the region (7.67 Ra) representing a MORB-like signature (Figs. 4 and 5).

It is noteworthy to mention that at least part of this nitrogen can be also derived from crustal sources such as shallow or deeply buried sediments and added to fluids during their migration towards the surface (Mitchell et al., 2010). However, it is difficult to obtain precise information about crustally derived nitrogen because the N_2/He ratios of our samples are fractionated by air contamination. Despite these limitations, we calculate the fraction of sediment-derived and MORB-derived nitrogen using the following relation (e.g. Fischer et al., 2002):

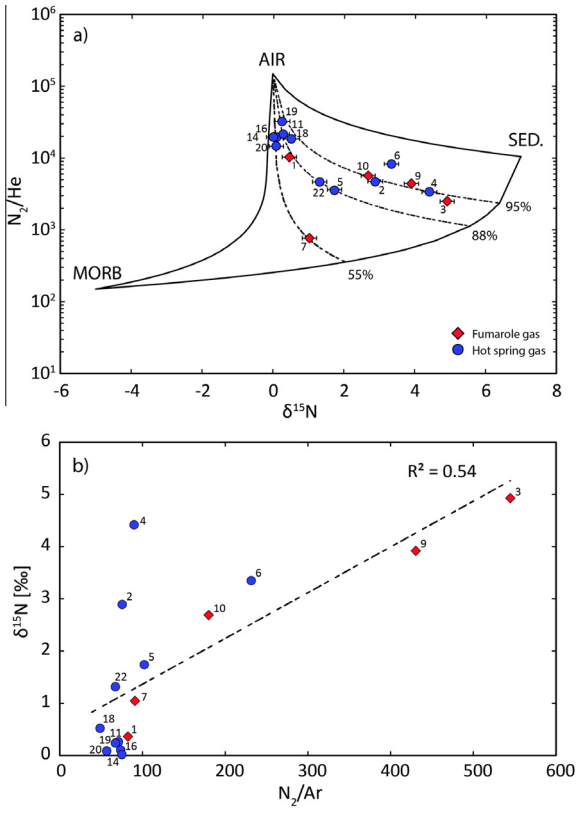

Fig. 6. Measured $\delta^{15}N$ (‰) versus N_2/He (a) and N_2/Ar (b) plots of SVZ fumaroles (red diamonds) and hot spring (blue circles) gas samples. In (a), MORB (−5‰, 1.5×10^2), sediments (+7‰, 1.05×10^4) and air (0‰, 1.489×10^5) values are reported (Sano et al., 2001; Fischer et al., 2002; Ozima and Podosek, 2002). Dotted lines reflect air addition to a mixture of mantle and sediment end-members (solid line), with percentages representing the amount of sediments in this mixture. (For interpretation of the references to colour in this figure legend, the reader is referred to the web version of this article.)

$$\delta^{15}N_C = (1 - f_{Sed})\delta^{15}N_{MORB} + f_{sed}\delta^{15}N_{Sed}$$

$$f_{MORB} + f_{Sed} = 1$$

where $\delta^{15}Nc$, $\delta^{15}N_{MORB}$, $\delta^{15}N_{Sed}$ are the corrected, MORB (−5 ± 2‰) and sediments (+7 ± 4‰) $\delta^{15}N$ values (Sano et al., 2001; Ozima and Podosek, 2002; Table 2). f_{MORB} and f_{sed} are the fractions of MORB-derived and sediment-derived nitrogen, respectively. In Fig. 7, the calculated $\delta^{15}Nc$ values were plotted as a function of Rc/Ra ratios. The air-corrected nitrogen values range between 1.60 (sample PL (7)) and 6.64 (sample PE (6)) and fit in the mixing line between MORB and sediments. Samples PL (7), LM (3), PM (4), JM (9) and AC (22) show a nitrogen contribution that is mainly a mixing between the mantle wedge and the subduction sediments in variable amounts, in agreement with Fig. 6a. In contrast, samples NC (1), TT (2), AV (5), PE (6), BT (10), VA (11), CO (18), TR (19), as also suggested by their lower Rc/Ra ratios, are most likely related to a significant contribution of nitrogen coming from shallow crustal sediments and from a deep crustal source (more than 10%). These samples showing noticeable crustal

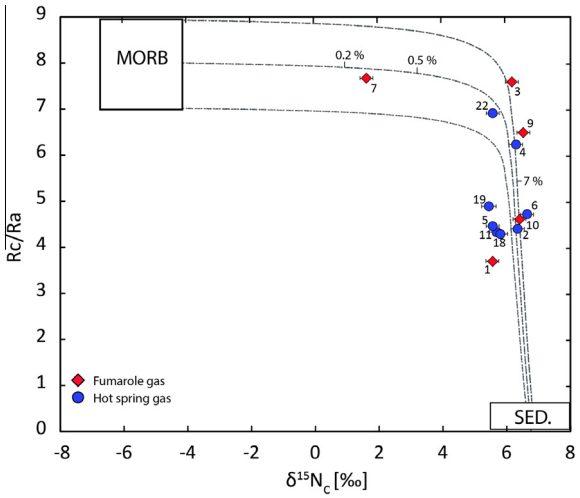

Fig. 7. $\delta^{15}Nc$ (‰) versus Rc/Ra plot of SVZ fumaroles (red diamonds) and hot springs (blue circles) gas samples. The MORB (−5 ± 2‰, 8 ± 1 Ra; Marty and Humbert, 1997; Sano et al., 2001) and sediments (+7 ± 3‰ and 0.05 Ra; Sano et al., 2001) end-members are shown. Dashed lines represent mixing between MORB and sediments. (For interpretation of the references to colour in this figure legend, the reader is referred to the web version of this article.)

nitrogen additions are correlated with the highest $^{87}Sr/^{86}Sr$ ratios in their host volcanoes (Fig. 4), and those occurring the northern portion of the studied region are also associated with faults that are misoriented for reactivation.

Crustal contamination also contributes to the variation of $\delta^{13}C$–CO_2 values and $CO_2/^3He$ ratios observed in SVZ volcanic/geothermal fluids, as presented in Figs. 3 and 4. The crustal contaminant has a $\delta^{13}C$ value between +6 and −28‰ (Faure, 1986; Oehlert and Swart, 2014) and a $CO_2/^3He$ ratio between 10^{12} and 10^{14} (Sano and Marty, 1995; Hoefs, 2009). In Fig. 8, $\delta^{13}C$ values are plotted along air-corrected $^3He/^4He$ (Rc/Ra) ratios for all the fumarole gas and hot spring samples. Helium and carbon isotopes show a clear positive correspondence. Two samples LM (3) and PL (7) show MORB-like signature consistent with a deep source for carbon. All the other fumarole gas samples (NC (1), JM (9), BT (10)) and four hot spring gas samples (PM (4), CU (8), VA (11), RB (13)) fall in a mixing field between MORB and crustal sediments, showing an important contribution of carbon from crustal sediments (Fig. 8). All the other bubbling gas and water-dissolved gas samples plot outside the mixing trend and show fractionation with relative loss of the heavier isotope that correlates with radiogenic ^4He addition.

The $CO_2/^3He$ ratios (e.g., Fig. 3) are lower than global arc average in most of the hot springs samples, with a minimum value at 5.08×10^5. Those low $CO_2/^3He$ values and the carbon isotope fractionation trend observed in the region seem to be controlled by secondary processes affecting the magmatic/hydrothermal systems, and that can drive the relative loss of CO_2 and a decrease in the $\delta^{13}C$ values (e.g., Fig. 8). Magmatic degassing and calcite precipitation may be responsible for such modifications on the isotopic composition of carbon; in fact, Ray et al.

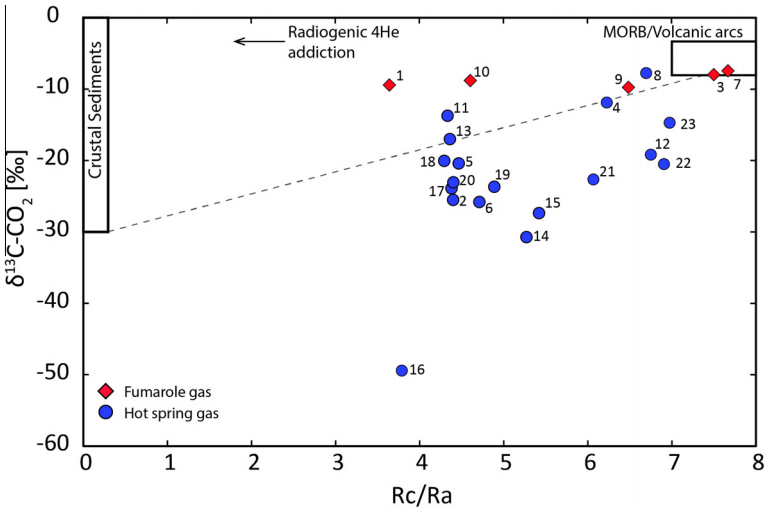

Fig. 8. Air-corrected $^3He/^4He$ ratios versus $\delta^{13}C–CO_2$ plot of SVZ fumaroles (red diamonds) and hot spring (blue circles) gas samples. Crustal sediments (+6 to −28‰, 0.05 Ra; Faure, 1986; Oehlert and Swart, 2014) and MORB (−6.5 ± 2.2‰, 8 ± 1 Ra; Marty et al., 1989, Farley and Neroda, 1998) fields are reported. Dashed line represent the lower limit of mixing field between MORB and crustal sediments. (For interpretation of the references to colour in this figure legend, the reader is referred to the web version of this article.)

(2009) hypothesized that these two processes are currently affecting geothermal emissions in the SVZ, with a stronger influence in the volatile-poor, hot-spring samples. As suggested by the correspondence between Rc/Ra values and $\delta^{13}C$ and $CO_2/^3He$ ratios (Fig. 8), magmatic degassing and calcite precipitation may be linked to increased residence times of fluids and crustal assimilation of the magmatic source (magmatic degassing). Therefore, it is likely that structurally-controlled vertical permeability exerts a significant role in modulating residence (and thus reaction) times of migrating fluids, conditioning their geochemical and isotopic signature through degassing or mixing with meteoric water (leading to calcite precipitation). These two processes will be discussed more precisely in further sections.

5.2. Mixing with meteoric fluids

As reported in previous studies (e.g., Sánchez et al., 2013), mixing with meteoric waters is one of the main processes affecting the chemical and isotopic signature of hydrothermal fluids in the SVZ. This process impacts the $^3He/^4He$ and $\delta^{15}N$ values by the addition of radiogenic ^4He and N_2, directly from atmospheric gases or from air-saturated water (ASW).

In Fig. 5, the R/Ra ratios are plotted along with $^4He/^{20}Ne$ ratios. The $^3He/^4He$ values are indicative of mixing between a MORB-like gas source, with addition of radiogenic ^4He by crustal contamination and air/air-saturated water (ASW). Bubbling gas and water-dissolved gas from hot springs samples in the southern part of the study area (38.5–40°S), and the fumarole gas sample NC (1) (Nevados de Chillan volcano in the northernmost part of the study area, Figs. 1 and 4) show in general a higher degree of contamination by air/ASW. Samples NC (1), VA (11), RB (13), QC (14), ME (15), PA (16), PF (17), CO (18), TR (19), CH (20) fall in a range between 6% and 20% of meteoric fluids in the mixture. Samples CU (8), PU (21) and RU (23), from the northern and southern part of the segment also fall within the same range. Samples PU (21) and RU (23), as commented above, have probably undergone direct air contamination during sampling. All other fumaroles and hot springs gas samples from the northern (37.5–38.5°S) and southern (41–42°S) segments present a degree of contamination that is significantly lower (<5%).

As we showed in the previous section, the N_2/He and N_2/Ar ratios in fumaroles and thermal fluids in the studied area cover an exceptionally wide range between 767.52 and 6.7×10^4, and 544.73 and 38.73 respectively. These ratios, when plotted along with $\delta^{15}N$ in Fig. 6a and b, show significant mixing with the atmospheric component. In Fig. 6b, datapoints show a wider dispersion in the mixing with air-derived nitrogen. The hot springs samples between 38.5°S and 40°S and the fumarole gas sample NC (1) show the highest degree of contamination by Air/ASW (Fig. 6b), in agreement with helium isotope data shown in Fig. 5.

Within a hydrothermal system, gas separation has the potential to fractionate both the gas ratio ($CO_2/^3He$) and the $\delta^{13}C–CO_2$ value (Giggenbach and Poreda, 1993; Barry et al., 2013). The observed $CO_2/^3He$ ratios in gas and water are different and consistent with gas separation. Helium is preferentially partitioned into the gas phase, whereas the more soluble CO_2 is concentrated in the aqueous liquid. This physical process produces an increase of $CO_2/^3He$ in residual water and can induce isotopic fractionation of $^{13}C/^{12}C$ ratios towards lower $\delta^{13}C–CO_2$ values (Vogel et al., 1970). As shown in Fig. 3, two bubbling gas samples (PM (4), CU (8)) show higher $CO_2/^3He$ values (5.78×10^{10} and 11.6×10^{10}) compared with their associated fumaroles in the Copahue and Pelehue geothermal areas (LM (3), PL (7). These values suggest He loss or CO_2 addition from local sediments. Furthermore, sample CU (8) has a $\delta^{13}C–CO_2$ value (−7.75‰) within the range of arc fumarolic

gases (Sano and Marty, 1995), while PM (4) show a lower value (−11.87‰). Both samples have an Rc/Ra ratio of 6.23 (PM (4)) and 6.69 (CU (8)) suggesting only a minor degree of crustal contamination. Therefore, the high $CO_2/^3He$ ratios may reflect both crustal contamination and/or vapor liquid partitioning processes, in close relation with the local scale fault-fracture meshes controlling the permeability in the Copahue and Pelehue geothermal systems (see Fig. 1).

5.3. Degassing and calcite precipitation

Figs. 3 show that more than half of the hot spring gas samples present low $CO_2/^3He$ ratios, in comparison to fumarole samples. This observation, also reported in previous studies in the SVZ (e.g., Ray et al., 2009), is suggestive of CO_2 loss from the magmatic/hydrothermal system (Giggenbach and Poreda, 1993). Ray et al. (2009) proposed two mechanisms that can possibly explain the low $CO_2/^3He$ ratios observed in SVG samples: (1) Magma degassing and (2) CO_2 loss driven by calcite precipitation. In the next paragraphs we evaluate these two processes for the studied segment.

Degassing of an andesitic-basaltic magma can produce a decrease in $CO_2/^3He$ in residual melt as well as the $\delta^{13}C$ values (Javoy et al., 1978; Hilton et al., 1998). For the He–CO_2 elemental fractionation, the fractionation factor (α) is defined as $(CO_2/^3He)_{vap}/(CO_2/^3He)_{melt}$, i.e., the inverse ratio of the solubility of He and CO_2 in the parental melt. For a tholeiitic melt, α is ~2.35 (Hilton et al., 1998). A preferential loss of CO_2 occurring during melt degassing will cause a decrease in the $CO_2/^3He$ ratio for the gas remaining in the melt, and a simultaneously decrease in the $\delta^{13}C$ values of the residual CO_2 (isotopic fractionation factor proposed is −4‰ corresponding to α: 0.996 Javoy et al., 1978).

Two models of degassing have been proposed: batch equilibrium (closed system) and Rayleigh distillation (open system). For these two models we assume an initial $CO_2/^3He$ of 11.95×10^9 and a $\delta^{13}C$ value of −8.95‰, corresponding to the average $CO_2/^3He$ and $\delta^{13}C$ values of the four fumarole gas samples falling in the volcanic-arc field in Fig. 3. By using the Rayleigh distillation equation, $CO_2/^3He_{residual} = (CO_2/^3He_{initial}) \times F^{(\alpha - 1)/\alpha}$, we calculate that the system would have needed to undergone a complete loss of CO_2 to achieve the lower $CO_2/^3He$ ratios measured in our samples (i.e., $CO_2/^3He = 5.08 \times 10^5$). Moreover, all our samples that have suffered a relative loss of CO_2 are below the Rayleigh distillation degassing curve in Fig. 9 (labeled "Rayleigh"). Therefore, it is likely that this process does not explain the low $CO_2/^3He$ ratios observed in the studied segment. Similarly, we tested a case of batch equilibrium degassing using the equations $\delta^{13}C_{residual} = \delta^{13}C_{initial} + (1 - F) \times 1000\ln(\alpha)$, and $CO_2/^3He_{residual} = (CO_2/^3He_{initial}) \times F^{(\alpha - 1)/\alpha}$ (after Javoy et al., 1978; Ray et al., 2009). As shown in Fig. 9, the batch degassing curve does not fit our data (labeled "Batch"). With this particular mode of degassing, the minimum possible values for $CO_2/^3He$ and $\delta^{13}C$ are 5.0×10^8 and −13‰, respectively (Fig. 9).

Consequently, and in agreement with previous studies by Ray et al. (2009) in the SVZ, we dismiss magmatic degassing as a viable process to explain the lower-than-arc-average $CO_2/^3He$ values in our samples. Another alternative mechanism to explain such low $CO_2/^3He$ values is CO_2 loss by calcite precipitation, occurring during cooling/mixing history of the hydrothermal system (e.g., Hilton et al., 1998). Fractionation between $CaCO_3$ and CO_2 gas can be calculated theoretically, and the temperature dependence for C soluble species with respect to $CaCO_3$ is well constrained (Bottinga, 1969). At temperatures less than 192 °C, calcite is enriched in ^{13}C relative to residual CO_2, thus the fractionation factors are −3‰ at 100 °C and −10‰ at 25 °C (Chacko et al., 2001). However, at temperatures greater than 192 °C, calcite is depleted in ^{13}C relative to residual CO_2 and the fractionation factor is around 0‰ (Sano and Marty, 1995; Ray et al., 2009; Barry et al., 2014). In Fig. 9, the plotted $CO_2/^3He$ and $\delta^{13}C$–CO_2 values illustrate the potential effect of calcite precipitation at two different temperatures, 25 °C and 192 °C (dashed lines). Our samples fall in a field defined by these two lines, showing that the low $CO_2/^3He$ and $\delta^{13}C$–CO_2 values measured in the studied samples can be explained by precipitation of calcite at various temperatures between 25 and 192 °C, as also previously proposed by Ray et al. (2009). Furthermore, evidence of calcite precipitation is present in several outcrop-scale dilational jogs along master and subsidiary faults of the LOFS (e.g., Pérez-Flores et al., 2014). The only two hot spring samples that do not fit this trend are BB (12) and PF (17). These samples were possibly subjected to hydrothermal degassing processes before calcite precipitation; therefore, these two samples may mark a starting point for the calcite precipitation lines which can be defined, as a first approximation, between the global arc-average and samples PM (4) and CU (8).

5.4. Conceptual model of fluid circulation

By combining the volcano-tectonic association of the studied segment of the SVZ (Table 3) with the helium, carbon and nitrogen isotope data presented in this study, a conceptual model that summarizes fluid circulation in the central part of SVZ is presented in Fig. 10.

The northern termination of the LOFS is characterized by a well-developed "horse-tail"-like accommodation zone (Fig. 1). The associated accommodation zone of such fault architectures, as asserted by many authors (Sibson, 1994, 1996; Kim et al., 2004; Rowland and Sibson, 2004; Rowland and Simmons, 2012), promote high vertical permeability and have long been recognized to play a key role as host structures focusing increased fluid flow in geothermal/hydrothermal systems. In the northern part of the studied segment (Figs. 1 and 10), the fumarole sample LM (3) and the hot spring sample PM (4) are associated with the Copahue geothermal area, which is set on a "pull apart" like basin, formed by the interplay of the LOFS and the Copahue-Antiñir Fault System (CAFS) (Melnick et al., 2006; Fig. 1; Sánchez et al., 2013). A few tens of kilometers towards the south, the occurrence of fumarole sample PL

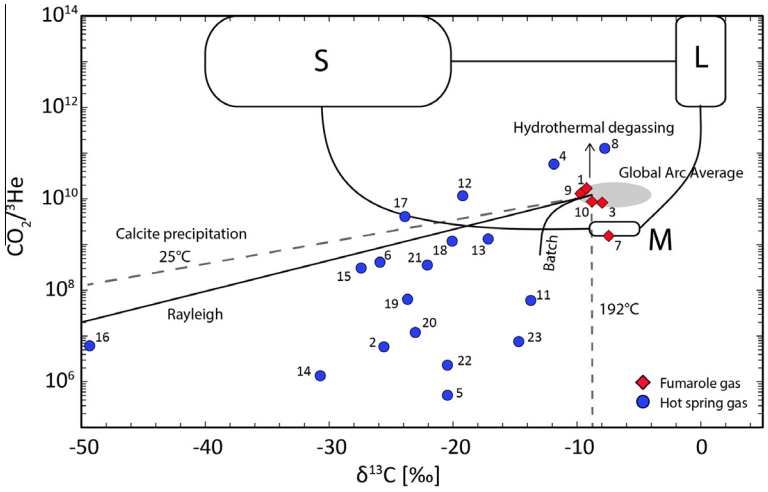

Fig. 9. $CO_2/^3He$ versus $\delta^{13}C$–CO_2 plot of SVZ fumaroles (red diamond) and hot springs (blue circles) gas samples compared to MORB (2×10^9, -6.5 ± 2.2‰; Marty et al., 1989; Sano and Marty, 1995; Sano and Williams, 1996), organic sediments (-30 ± 10‰, 1×10^{13}; Sano and Marty, 1995; Hoefs, 2009) and marine limestone (1×10^{13}; 0 ± 2‰; Sano and Marty, 1995; Hoefs, 2009). Dashed lines represent trajectories for CO_2 loss by calcite precipitation at a temperature of 25 °C (fractionation factor = −10‰) and 192 °C (fractionation factor = 0‰). The starting point is $CO_2/^3He = 11.95 \times 10^9$ and a $\delta^{13}C = -8.95$‰. The vertical arrow represent the direction for hydrothermal degassing process. Rayleigh distillation and batch equilibrium curves are also shown. (For interpretation of the references to colour in this figure legend, the reader is referred to the web version of this article.)

(7) in the Pelehue area and the hot spring sample CU (8) in Coyuco is controlled by a series of NE-striking extensional and transtensional faults that are located east of the main volcanic arc (Fig. 1). There are no recognized volcanic centers close to these two thermal manifestations, which seem to be controlled directly by the fault splays of the LOFS (Fig. 1). The fumaroles gas samples LM (3) and PL (7), both labeled as "a" in Fig. 10, show MORB-like $^3He/^4He$ ratios indicating primitive sources and no significant degrees of crustal contamination (Figs. 4 and 5). Despite this common feature, carbon and nitrogen isotope data point to two completely different signatures for these two systems. $CO_2/^3He$, $\delta^{13}C$–CO_2 (Fig. 9) and $\delta^{15}N$ values (Fig. 6a) show a typical volcanic arc signature for LM (3) sample. Carbon and nitrogen signatures most likely originated, in this case, by mixing between mantle and sediments derived from the slab, with almost no contribution from continental crust and mixing with meteoric water. In contrast, the PL (7) sample displays a predominant MORB-like carbon signature and a lower nitrogen contribution from the slab than all the other samples (55%, Fig. 6a), with no nitrogen addition from the continental crust. This signature appears consistent with the retro-arc location of the fumarolic field of Pelehue, 20 km far from the closest known eruptive center, and almost 50 km eastward from the present-day location of the active volcanic arc. Water-dissolved gas samples PM (4) and CU (8), also spatially associated with the horse-tail northern termination of the LOFS, are the only two samples affected by hydrothermal degassing and show more crustal additions of helium, nitrogen and carbon with respect to the fumaroles LM (3) and PL (7). The carbon isotope signatures indicate that these hot springs have suffered a vapor–liquid separation and partial gas-phase loss, suggesting that crustal contamination processes are more easily perceived in such volatile-poor samples. These are among the least contaminated samples in the whole region, with air-corrected $^3He/^4He$ ratios ranging between 6 and 7.

Further south, in the central part of the studied segment ("b", Fig. 10), fumaroles and hot springs are spatially associated with stratovolcanoes controlled by transtensional NE-striking faults (e.g., Sollipulli volcano; Fig. 1) or by the intersection between NE- (LOFS) and NW-striking transpressive faults (ALFS) (e.g., Tolhuaca and Cordon Caulle volcanoes; Figs. 1 and 10). These volcanic systems show a higher degree of crustal contamination, with $^{87}Sr/^{86}Sr$ ratios higher than lavas related to volcanoes in the northernmost part of the segment ("a", Fig. 10). The associated thermal manifestations in this area are also characterized by a minor degree of crustal contamination of their magmatic source(s). As shown in Fig. 4, the Rc/Ra ratios in samples JM (9), BB (12), PU (21), AC (22) and RU (23) are among the highest in the region (Rc/Ra ~ 6–7) and correlate with low $^{87}Sr/^{86}Sr$ ratios in their host stratovolcanoes. The nitrogen isotope signature suggests mixing between MORB and sediments, with minor contribution from continental crust (Fig. 8). $CO_2/^3He$ and $\delta^{13}C$–CO_2 show the typical volcanic-arc signature for fumarole sample JM (9), whereas the water-dissolved gas samples are slightly affected by CO_2 loss and $\delta^{13}C$–CO_2 fractionation for calcite deposition (Fig. 9).

Finally, the case "c" in Fig. 10 represent all those fumaroles and hot springs associated with stratovolcanoes that are controlled by pure transpressive NW-striking faults (Nevado de Chillan, Villarica and Mocho-Choshuenco volcanoes; Fig. 1, presenting the highest degrees of crustal contamination (NC (1), BT (10), VA (11), RB (13), QC (14), ME (15), PA (16), PF (17), CO (18), TR (19), CH (20)) and the hot springs spatially related with transpressional fault-fracture zones that do not permit a high vertical permeability (TT (2), AV (5), PE (6)).

Table 3
Volcano-tectonic associations along the studied segment of the SVZ.

Group	Name	Location	Description	References	Samples
a: LOFS northern transtensional termination	Copahue-Caviahue volcanic complex	37° 51′S	The Caviahue-Copahue volcanic complex is located at the northern termination of the LOFS in a "horsetail"-like accommodation zone. The area is limited by two major fault zones, the Copahue–Antiñir thrust system to the north and the main branch of the LOFS, to the south, which locally form pull-apart structures. Magmatic products associated with active Copahue volcano vary from basaltic-trachyandesites to trachyandesites. Several NE-striking strike-slip faults and NE-striking half-graben are located within 40 km to the south of the Caviahue-Copahue complex. One of these structure is forming the Pelehue valley, located in backarc position with respect of the present day active volcanic arc	Melnick et al. (2006), Varekamp et al. (2006), Rosenau et al. (2006), Pérez-Flores et al. (2014)	LM (3), PM (4)
	Pelehue valley	38° 07′S			PL (7), CU (8)
b: LOFS dominant and interplay between LOFS and ALFS	Sollipulli volcano	38° 58′S	Stratovolcanoes and pyroclastic cones that form NE–SW alignments. Mostly basalts have been erupted from these arrays but stratovolcanoes evacuated also dacites or rhyolites	Gilbert et al. (1996); Cembrano and Lara (2009); Lachowycz et al. (2015)	RU(23)
	Antillanca volcanic complex	40° 46′S			BB (12)
	Tolhuaca volcano	38° 19′S	Stratovolcanoes or clusters of stratovolcanoes controlled by the interplay of NW-striking sinistral-reverse faults of the ALFS and NE- to NNE-striking dextral-normal faults of LOFS. Volcanic edifices show no asymmetry of the base but they can display flank vents in preferred NW orientation. Magmatic products present a wide compositional range from basaltic to dacitic and rhyolitic	Lara et al. (2006), Cembrano and Lara (2009), Pérez-Flores et al. (2014)	JM (9)
	Puyehue-Cordón Caulle volcanic complex	40° 35′S			PU (21), AC (22)
c: Dominant ALFS	Nevado de Chillan volcano	36° 52′S	Stratovolcanoes built on top of the of NW-striking sinistral-reverse faults from the ALFS. LOFS is represented by the NNE-striking master fault. Volcanic edifices show no or slightly asymmetry of the base and they can display flank vents in NW-preferred orientation. Compositions cover a wide range from basalts to rhyolites	Melnick et al. (2006), Cembrano and Lara (2009), Sánchez et al. (2013)	NC (1)
	Sierra Nevada volcano	38° 34′S			BT (10), VA (11)
	Villarica-Quetrupillan-Lanin volcanic alignment	39° 25″–39° 38″S			RB (13), QC (14), ME (15), PA (16), PF (17), CO (18), TR (19), CH (20)
	Mocho Choshuenco volcano	39° 56′S			
	Trapa Trapa thermal spring	37° 41′S	Thermal springs related NW-trending faults of the ALFS. The hot springs are spatially associated with Callaqui stratovolcano, a N60E elongated volcanic fissure, with parasites and pyroclastic cones alignment in the same direction. The composition of erupted products from Callaqui volcano is mainly basaltic-andesitic	Moreno et al. (1984), Potent (2003), Cembrano and Lara (2009), Radic (2010)	TT (2)
	Avellano thermal spring	37° 55′S			AV (5)
	Pemehue thermal spring	38° 4′S			PE (6)

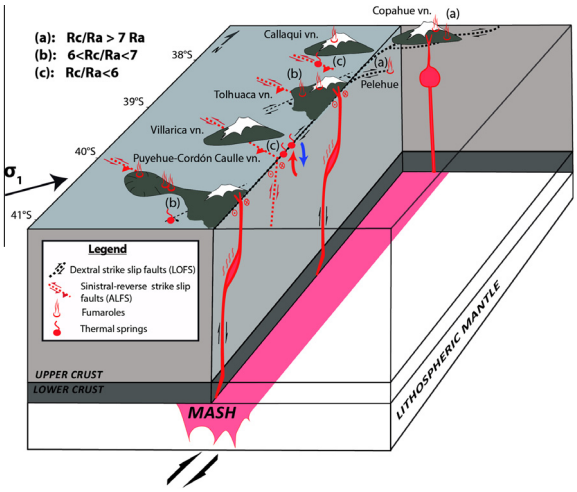

Fig. 10. Block model showing the structurally-controlled fluid circulation model proposed for the studied segment of the Southern Volcanic Zone. Black and red dashed lines represent the LOFS and ALFS, respectively. Fumaroles and hot springs are represented along with their relation to volcanic edifices and structural settings. Blue and red arrows represent the mixing between deep and meteoric fluids. Sigma 1 (σ1) represent the maximum regional stress field. Helium ratios (Rc/Ra) ranges are shown in the upper left. (For interpretation of the references to color in this figure legend, the reader is referred to the web version of this article.)

The hot springs located between Villarica and Mocho-Choshuenco volcanoes (Fig. 5, and Fig. 6a and b) also show the highest degree of mixing with meteoric water. As also hypothesized by Sánchez et al. (2013), most of these thermal springs are associated with the main traces of the LOFS that, due to their high vertical permeability, allow a deeper circulation of the meteoric fluids, further increasing the dilution process in this already humid and rainy region. The $CO_2/^3He$ and $\delta^{13}C–CO_2$ indicate a significant loss of CO_2 and ^{13}C for calcite precipitation in almost all the case "c" samples, except for fumaroles gas samples NC (1) and BT (10) and hot spring gas samples VA (11) and RB (13) (Fig. 7). As discussed in Section 5.4, the CO_2 loss driven by calcite precipitation correlate with $^3He/^4He$ ratios. This trend shows how calcite precipitation may be enhanced by the low permeability vertical pathways along the LOFS; this process can occur during the cooling/mixing history of the hydrothermal system that increase the reaction time with country rock and the cooling of magmatic vapor, and/or by mixing with cold and shallow infiltrating waters.

6. CONCLUDING REMARKS

Our combined isotopic, geochemical and structural data indicate that the NNE-striking intra-arc, strike-slip Liquiñe-Ofqui Fault System (LOFS) and the NW-striking Arc-oblique Long-lived Basement Fault System (ALFS) exert a fundamental control on the helium, nitrogen and carbon isotope signature of thermal manifestations in the Chilean Andes between ~37°S and 41°S. In this segment of the Southern Volcanic Zone (SVZ), thermal fluids are characterized by a wide range of $^3He/^4He$, $CO_2/^3He$, $\delta^{13}C–CO_2$ and $\delta^{15}N$ values. We explain these variations by linking the geochemical data of gas in fumaroles and thermal spring water, to a wider geological context that includes the regional distribution of fault-fracture meshes and the isotopic variation of source magmas.

The first order control on helium, carbon and nitrogen isotopes signatures observed in the studied segment seems to be largely dominated by the degree of crustal assimilation of the magmatic sources, which is in turn controlled by the LOFS and ALFS. As shown in Fig. 4, the air-corrected $^3He/^4He$, $\delta^{13}C–CO_2$ and $\delta^{15}N$ fumarole gas data show a strong correspondence with the $^{87}Sr/^{86}Sr$ ratios of lavas from hosting volcanic systems. The thermal spring gas data also show a similar correspondence, although partly masked by secondary processes. Our observations also indicate that the magmatic sources of hydrothermal fluids in the region are highly variable at the regional scale, and more primitive signatures are most likely transmitted to the shallow volcanic/geothermal environment along the NNE-striking LOFS.

In contrast, the isotopic signatures of gases in thermal manifestations along the arc-oblique, NW-striking ALFS, show a higher degree of crustal contamination. Considering the fact that the ALFS inhibit vertical fluid permeability due to its misorientation with respect to the prevailing regional stress field, the $^3He/^4He$, $\delta^{13}C–CO_2$ and $\delta^{15}N$ data records crustal contributions related to increased fluid/rock interaction and higher residence times.

Whereas the ALFS promote the formation of long-lived, more evolved high-enthalpy hydrothermal reservoirs (e.g., Tolhuaca geothermal field), the LOFS allow a higher vertical permeability of hydrothermal fluids from more primitive, MORB-like magmatic sources. These large-scale structures are effective loci for enhanced fluid flow, providing a "background" $^3He/^4He$ signal in the area that exceeds by far the crustal helium signature of 0.05 Ra. This crustal-scale fault system also promote the deep circulation of meteoric fluids, as occurring for thermal springs between 38.5°S and 40°S, that partially masks the deep $\delta^{13}C–CO_2$ and $\delta^{15}N$ signatures due to shallow processes such as mixing with meteoric water and calcite precipitation.

ACKNOWLEDGEMENTS

This study was funded by a FONDECYT grant #1130030 to Martin Reich. Additional funding was provided by FONDAP project 15090013 "Centro de Excelencia en Geotermia de los Andes, CEGA". The authors acknowledge support through the MSI "Millennium Nucleus for Metal Tracing Along Subduction" (NC130065). This work was also partially supported by Grant-in-Aid for Science Research (15H05830) from MEXT, Japan, and a FONDECYT Iniciación grant (#11130351). Daniele Tardani thanks financial support provided by the MECESUP program through a Ph.D. scholarship. The authors would also like to thank the "Ente Provincial Termas del Neuquen" and other natural thermal spas that granted permission to take samples for this study.

Finally, we acknowledge chief editor Marc Norman and associate editor Jeffrey C. Alt for handling the manuscript. Daniele Pinti and Peter Barry are acknowledged for their helpful comments and suggestions.

REFERENCES

Adriasola A. C., Thomson S. N., Brix M. R., Hervé F. and Stockhert B. (2006) Postmagmatic cooling and Late Cenozoic denudation of the North Patagonian Batholith in the Los Lagos Region of Chile, 41°S–42°S. *Int. J. Earth Sci.* **95**, 504–528.

Agusto M., Tassi F., Caselli A. T., Vaselli O., Rouwet D., Capaccioni B., Caliro S., Chiodini G. and Darrah T. (2013) Gas geochemistry of the magmatic-hydrothermal fluid reservoir in the Copahue-Caviahue Volcanic Complex (Argentina). *J. Volcanol. Geotherm. Res.* **257**, 44–56.

Alam M. A., Sánchez P. and Parada M. A. (2010) Interplay of volcanism and structural control in defining the geothermal system(s) along the Liquiñe-Ofqui Fault Zone, in the south-central Chile. *Geotherm. Resour. Council (GRC) Trans.* **34**, 747–750.

Angermann D., Klotz J. and Reigber C. (1999) Space-geodetic estimation of the Nazca-South America Euler vector. *Earth Planet. Sci. Lett.* **171**(3), 329–334.

Barry P. H., Hilton D. R., Halldórsson S. A., Hahm D. and Marti K. (2012) High precision nitrogen isotope measurements in oceanic basalts using a static triple collection noble gas mass spectrometer. *Geochem. Geophys. Geosyst.* **13**, Q01019.

Barry P. H., Hilton D. R., Fischer T. P., De Moor J. M., Mangasini F. and Ramirez C. (2013) Helium and carbon isotope systematics of cold "mazuku" CO_2 vents and hydrothermal gases and fluids from Rungwe Volcanic Province, southern Tanzania. *Chem. Geol.* **339**(2013), 141–156.

Barry P. H., Hilton D. R., Furi E., Halldórsson S. A. and Gronvold K. (2014) Carbon isotope and abundance systematics of Icelandic geothermal gases, fluids and subglacial basalts with implications for mantle plume-related CO_2 fluxes. *Geochim. Cosmochim. Acta* **134**(2014), 74–99.

Blenkinsop T. G. (2008) Relationships between faults, extension fractures and veins, and stress. *J. Struct. Geol.* **30**, 622–632.

Bottinga Y. (1969) Calculated fractionation factors for carbon and hydrogen isotope exchange in the system calcite-CO2-graphite–methane–hydrogen and water vapor. *Geochim. Cosmochim. Acta* **33**, 49–64.

Cembrano J. and Moreno H. (1994) Geometría y naturaleza contrastante del volcanismo Cuaternario entre los 38° S y 46° S: ¿Dominios compresionales y tensionales en un régimen transcurrente?. In *Congreso Geológico Chileno No. 7, Actas*, Vol. 1, pp. 240–244. Congreso Geológico Chileno, No. 7, Actas. Universidad de Concepción, Chile.

Cembrano J., Hervé F. and Lavenu A. (1996) The Liquiñe-Ofqui fault zone: a long-lived intra-arc fault Zone in southern Chile. *Tectonophysics* **259**, 55–66.

Cembrano J., Shermer E., Lavenu A. and Sanhueza A. (2000) Contrasting nature of deformation along an intra-arc shear zone, the Liquiñe-Ofqui fault zone, southern Chilean Andes. *Tectonophysics* **319**, 129–149.

Cembrano J. and Lara L. (2009) The link between volcanism and tectonics in the southern volcanic zone of the Chilean Andes: A review. *Tectonophysics* **471**, 96–113.

Chacko T., Cole D. R. and Horita J. (2001) Equilibrium oxygen, hydrogen and carbon isotope fractionation factors applicable to geologic systems. In *Stable Isotope Geochemistry. Rev Mineral Geochem*, 43 (eds. J. W. Valley and D. R. Cole), pp. 1–81.

Charrier R., Baeza O., Elgueta S., Flynn J., Gans P., Kay S., Muñoz N., Wyss A. and Zurita E. (2002) Evidence for Cenozoic extensional basin development and tectonic inversion south of the flat-slab segment, southern central Andes, Chile (33°–36°S.L.). *J. South Am. Earth Sci.* **15**, 117–139.

Clor L. E., Fischer T. P., Hilton D. R., Sharp Z. D. and Hartono U. (2005) Volatile and N isotope chemistry of the Molucca Sea collision zone: tracing source components along the Sangihe Arc, Indonesia. *Geochem. Geophys. Geosyst.* **6**, Q03J14.

Cox S. F. (2010) The application of failure mode diagrams for exploring the roles of fluid pressure and stress states in controlling styles of fracture-controlled permeability enhancement in faults and shear zones. *Geofluids* **217–233**. http://dx.doi.org/10.1111/j.1468-8123.2010.00281.x.

Craig H., Lupton J. E. and Horibe Y. (1978) A mantle helium component in Circum-Pacific volcanic gases: Hakone, the Marianas, and Mr. Lassen. In *Terrestrial Rare GasesE.C. Advances in Earth and Planetary Science* (eds. Alexander and M. Ozima). Academic Publication, Japan, pp. 3–16.

Davidson J., Dungan M. A., Ferguson K. M. and Colucci M. T. (1987) Crust–magma interactions and the evolution of arc magmas: the San Pedro-Pellado volcanic complex, southern Chilean Andes. *Geology* **15**, 443–446.

Deruelle B., Harmon R. S. and Moorbath S. (1983) Combined Sr–O isotopes relationships and petrogénesis of Andean volcanics of South America. *Nature* **302**, 814–816.

Dobson P. F., Kennedy B. M., Reich M., Sánchez P., Morata D. (2013) Effects of volcanism, crustal thickness and large scale faulting on the He isotope signatures of geothermal systems in Chile. Thirty-Eighth Workshop on Geothermal Reservoir Engineering Stanford University, Stanford, California, February 11–13, 2013, SGP-TR-198.

Farley K. A. and Neroda E. (1998) Noble gases in the Earth's mantle. *Annu. Rev. Earth Planet. Sci.* **26**, 189–218.

Fairley J. P. and Hinds J. J. (2004) Rapid transport pathways for geothermal fluids in an active Great Basin fault zone. *Geology* **32**, 825–828.

Faulkner D. R., Jackson C. A. L., Lunn R. J., Schlische R. W., Shipton Z. K., Wibberley C. A. J. and Withjack M. O. (2010) A review of recent developments concerning the structure, mechanics and fluid flow properties of fault zones. *J. Struct. Geol.* **32**, 1557–1575.

Faure G. (1986) *Principles of Isotope Geology*, 2nd ed. John Wiley and Sons Inc, Canada, p. 501.

Fischer T. P., Giggenbach W. F., Sano Y. and Williams S. N. (1998) Fluxes and sources of volatiles discharged from Kudryavy, a subduction zone volcano, Kurile Islands. *Earth Planet. Sci. Lett.* **160**, 81–96.

Fischer T. P. et al. (2002) Subduction and recycling of nitrogen along the Central American margin. *Science* **297**, 1154–1157.

Folguera A., Ramos V. A. and Melnick D. (2002) Partición de la deformación en la zona del arco volcánico de los Andes neuquinos (36–39°S) en los últimos 30 millones de años. *Rev. Geol. Chile* **29**(2), 151–165.

Gerlach D., Frey F., Moreno H. and López-Escobar L. (1988) Recent volcanism in the Puyehue-Cordón Caulle Region, Southern Andes, Chile (40.5°S): petrogénesis of evolved lavas. *J. Petrol.* **29**, 333–382.

Giggenbach W. F., Goguel R. L. (1989) Methods for the collection and analysis of geothermal and volcanic water and gas samples. Department of Scientific and Industrial Research, Chemistry Division. Petone, New Zealand.

Giggenbach W. F. and Corrales S. R. (1992) Isotopic and chemical composition of water and steam discharges from volcanic-magmatic-hydrothermal systems of the Guanacaste Geothermal Province, Costa Rica. *Appl. Geochem.* **7**, 309–332.

Giggenbach W. F. and Glover R. B. (1992) Tectonic regime and major processes governing the chemistry of water and gas discharges from the Rotorua geothermal field, New Zealand. *Geothermics* **21**, 121–140.

Giggenbach W. F. and Poreda R. J. (1993) Helium isotopic and chemical composition of gases from volcanic hydrothermal systems in the Philippines. *Geothermics* **22**, 369e–380e.

Gilbert J. S., Stasiuk M. V., Lane S. J., Adam C. R., Murphy M. D., Sparks R. S. J. and Naranjo J. A. (1996) Non-explosive constructional evolution of the ice-filled caldera at VolcánSollipulli. *Chile. Bull. Volcanol.* **58**, 67–83. http://dx.doi.org/10.1007/s004450050127.

Glodny J., Gräfe K., Echtler H. and Rosenau M. (2008) Mesozoic to Quaternary continental margin dynamics in South-Central Chile (36°–42°S): the apatite and zircon fission track perspective. *Int. J. Earth Sci.* **97**, 1271–1291.

Graf T. and Therrien R. (2009) Stable-unstable flow of geothermal fluids in fractured rock. *Geofluids* **9**, 138–152.

Graham D. W. (2002) Noble gas isotope geochemistry of mid-ocean ridge and ocean island basalts: Characterization of mantle source reservoirs. *Rev. Mineral. Geochem.* **47**, 247–318.

Gudmundsson A., Simmenes T. H., Larsen B. and Philipp S. L. (2010) Effects of internal structure and local stresses on fracture propagation, deflection, and arrest in fault zones. *J. Struct. Geol.* **32**, 1643–1655.

Hauser A. (1997) Catastro y caracterización de las fuentes de agues minerals y termales de Chile. Boletin, vol. 50. Servicio Nacional de Geologia y Mineria-Chile, p. 89.

Hickey-Vargas R., Moreno H., López Escobar L. and Frey F. (1989) Geochemical variations in Andean basaltic and silicic lavas from the Villarrica-Lanín volcanic chain (39.5°S): an evaluation of source heterogeneity, fractional crystallization and crustal assimilation. *Contrib. Miner. Petrol.* **103**, 361–386.

Hildreth W. and Moorbath S. (1988) Crustal contributions to arc magmatism in the Andes of Central Chile. *Contrib. Miner. Petrol.* **98**(4), 455–489. http://dx.doi.org/10.1007/BF00372365.

Hilton D. R., Hammerschmidt K., Teufel S. and Friedrichsen H. (1993) Helium isotope characteristics of Andean geothermal fluids and lavas. *Earth Planet. Sci. Lett.* **120**, 265–282.

Hilton D. R., McMurtry G. M. and Goff F. (1998) Large variations in vent fluid $CO_2/^3He$ ratios signal rapid changes in magma chemistry at Loihi Seamount, Hawaii. *Nature* **396**, 359–362.

Hilton D. R., Fischer T. P. and Marty B. (2002) Noble gases and volatile recycling at subduction zones. In *Reviews in Mineralogy and Geochemistry: Noble Gases in Geochemistry and Cosmochemistry*, vol. 47 (eds. D. P. Porcelli, C. J. Ballentine and R. Wieler), pp. 319–370.

Hoefs J. (2009) Stable Isotope Geochemistry, p. 288.

Javoy M., Pineau F. and Iiyama I. (1978) Experimental determination of the isotopic fractionation between gaseous CO2 and carbon dissolved in tholeiitic magma; a preliminary study. *Contrib. Mineral. Petrol.* **67**, 35–39.

Karlstrom K. E., Crossey L. J., Hilton D. R. and Barry P. H. (2013) Mantle ^3He and CO_2 degassing in carbonic and geothermal springs of Colorado and implications for neotectonics of the Rocky Mountains. *Geology* **41**(4), 495–498. http://dx.doi.org/10.1130/G34007.1.

Kay S. M., Godoy E. and Kurtz A. (2005) Episodic arc migration, crustal thickening, subduction erosion, and magmatism in the south-central-Andes. *Geol. Soc. Am. Bull.* **117**, 67–88. http://dx.doi.org/10.1130/B25431.1.

Kennedy B. M., Kharaka Y. K., Evans W. C., Ellwood A., DePaolo D. J., Thordsen J., Ambats G. and Mariner R. H. (1997) Mantle fluids in the San Andreas fault system, California. *Science* **278**, 1278–1281.

van Kennedy B. M. and Soest M. C. (2005) Regional and local trends in helium isotopes, Basin and Range Province, western North America: evidence for deep permeable pathways. *Geotherm. Resour. Council Trans.* **29**, 263–268.

Kim Y. S., Peacock D. C. P. and Sanderson D. J. (2004) Fault damage zones. *J. Struct. Geol.* **26**(2004), 503–517.

Lachowycz S. M., Pyle D. M., Gilbert J. S., Mather T. A., Mee K., Naranjo J. A. and Hobbs L. K. (2015) Glaciovolcanism at Volcán Sollipulli, southern Chile: Lithofacies analysis and interpretation. *J. Volcanol. Geoth. Res.* **303**, 59–78.

Lahsen A., Muñoz N., Parada M. A. (2010) Geothermal development in Chile. Proceedings World Geothermal Congress, Bali, Indonesia, Paper N° 25.

Lange D., Cembrano J., Rietbrock A., Haberland C., Dahm T. and Bataille K. (2008) First seismic record for intra-arc strike-slip tectonics along the Liquiñe-Ofqui fault zone at the obliquely convergent plate margin of the southern Andes. *Tectonophysics* **455**, 14–24.

Lara L. E., Naranjo J. A. and Moreno H. (2004) Rhyodacitic fissure eruption in Southern Andes (Cordón Caulle; 40.5°S) after the 1960 (Mw: 9.5) Chilean earthquake: a structural interpretation. *J. Volcanol. Geotherm. Res.* **138**, 127–138.

Lara L. E., Lavenu A., Cembrano J. and Rodríguez C. (2006) Structural controls of volcanism in transversal chains: resheared faults and neotectonics in the Cordón Caulle-Puyehue area (40.5°S), Southern Andes. *J. Volcanol. Geotherm. Res.* **158**, 70–86.

Lavenu A. and Cembrano J. (1999) Compressional and transpressional-stress pattern for Pliocene and Quaternary brittle deformation in fore arc and intra-arc zones (Andes of Central and Southern Chile). *J. Struct. Geol.* **21**, 1669–1691.

López-Escobar L., Cembrano J. and Moreno H. (1995) Geochemistry and tectonics of the Chilean Southern Andes basaltic quaternary volcanism (37–46°S). *Rev. Geol. Chile* **22**(2), 219–234.

Mabry J., Lan T., Burnard P. and Marty B. (2013) High-precision helium isotope measurements in air. *J. Anal. At. Spectrom.* **28** (12), 1903–1910.

Manning C. E. and Ingebritsen S. E. (1999) Permeability of the continental crust: implications of geothermal data and metamorphic systems. *Rev. Geophys.* **37**, 127–150.

Marty B. and Humbert F. (1997) Nitrogen and argon isotopes in oceanic basalts. *Earth Planet. Sci. Lett.* **152**, 101–112.

Marty B. and Jambon A. (1987) $C/^3He$ in volatile fluxes from the solid Earth: Implication for carbon geodynamics. *Earth Planet. Sci. Lett.* **83**, 16–26.

Marty B., Jambon A. and Sano Y. (1989) Helium isotopes and CO_2 in volcanic gases of Japan. *Chem. Geol.* **76**, 25–40.

McMillan N. J., Harmon R. S., Moorbath S., Lopez-Escobar L. and Strong D. (1989) Crustal sources involved in continental arc magmatism: a case study of Volcan Mocho– Choshuenco, southern Chile. *Geology* **17**, 1152–1156.

Melnick D., Folguera A. and Ramos V. A. (2006) Structural control on arc volcanism: the Copahue-Agrio complex, South-Central Andes (37°50´S). *J. South Am. Earth Sci.* **22**, 66–88.

Micklethwaite S. and Cox S. F. (2004) Fault-segment rupture, aftershock-zone fluid flow, and mineralization. *Geology* **32**, 813–816.

Micklethwaite S., Sheldon H. A. and Baker T. (2010) Active fault and shear processes and their implications for mineral deposit formation and discovery. *J. Struct. Geol.* **32**, 151–165.

Mitchell E. C., Fischer T. P., Hilton D. R., Hauri E. H., Shaw A. M., de Moor J. M., Sharp Z. D. and Kazahaya K. (2010) Nitrogen sources and recycling at subduction zones: insights fromthe Izu-Bonin-Mariana arc. *Geochem. Geophys. Geosyst.* **11**, Q02X11.

Moreno H., Lahsen A., Thiele R. and Varela J. (1984) Estudio del Volcán Callaqui, Contrato 01CB-01. Geología del Área del Volcán Callaqui, Escala 1:50.000. Endesa. Departamento de Geología y Geofísica, Facultad de Ciencias Físicas y Matemáticas, Universidad de Chile.

Morrison P. and Pine J. (1955) Radiogenic origin of the helium isotopes in rock. *Ann. N Y Acad. Sci.* **62**, 71–92.

Oehlert A. M. and Swart P. K. (2014) Interpreting carbonate and organic carbon isotope covariance in the sedimentary record. *Nat. Commun.* **5**, 4672. http://dx.doi.org/10.1038/ncomms5672.

Ozima M. and Podosek F. A. (2002) *Noble Gas Geochemistry*. Cambridge University Press, p. 300.

Parada M. A., López-Escobar L., Oliveros V., Fuentes F., Morata D., Calderón M., Aguirre L., Féraud G., Espinoza F., Moreno H., Figueroa O., Muñoz-Bravo J., Troncoso Vásquez R. and Stern C. R. (2007) Andean magmatism. In *The Geology of Chile, 21–114* (eds. T. Moreno and W. Gibbons). The Geological Society, London, pp. 115–146.

Pérez Y. D. (1999) Fuentes de aguas termales de la Cordillera Andina del Centro-Sur de Chile (39–42oS). Boletin, vol. 54. Servicio Nacional de Geologia y Mineria, p. 65.

Pérez-Flores P., Cembrano J., Sánchez P. (2014) Local Stress fields and paleo-fluid distribution within a transtensional duplex: An example from the northern termination of the Liquiñe-Ofqui Fault System. Abstract T26C 4697 AGU fall Meeting San Francisco, EE.UU.

Potent S. and Reuther C. (2001) Neogene Deformations prozesse im aktiven magmatischem Bogen Südzentralchiles zwischen 37° und 39°S. *Mitteilungen Geologisch-Paläontologisches Institut Universität Hamburg*, Vol. 85, pp. 1–22.

Potent S. (2003) Kinematik und Dynamik neogener Deformationsprozesse des südzentralchilenischen Subduktionssystems, nö rdlichste Patagonische Anden (37–40S). Ph. D. thesis, Universität Hamburg, p.169.

Pritchard M. E., Jay J. A., Aron F., Henderson S. T. and Lara L. E. (2013) Subsidence at southern Andes volcanoes induced by the 2010 Maule, Chile earthquake. *Nat. Geosci.* **6**, 632–636.

Radic J. P. (2010) Las cuencas cenozoicas y su control en el volcanismo de los Complejos Nevados de Chillán y Copahue-Callaqui (Andes del Sur, 36–39°S). *Andean Geol.* **37**, 220–246.

Ray M. C., Hilton D. R., Munoz J., Fischer T. P. and Shaw A. M. (2009) The effects of volatile recycling, degassing and crustal contamination on the helium and carbon geochemistry of hydrothermal fluids from the Southern Volcanic Zone of Chile. *Chem. Geol.* **266**(1–2), 38–49.

Rosenau M., Melnick D. and Echtler H. (2006) Kinematic constraints on intra-arc shear and strain partitioning in the Southern Andes between 38°S and 42°S latitude. *Tectonics* **25**, TC4013.

Rowland J. V. and Sibson R. H. (2004) Structural controls on hydrothermal flow in a segmented rift system, Taupo Volcanic Zone, New Zealand. *Geofluids* **4**, 259–283. http://dx.doi.org/10.1111/j.1468-8123.2004.00091.x.

Rowland J. V. and Simmons S. F. (2012) Hydrologic, magmatic, and tectonic controls on hydrothermal flow, Taupo volcanic zone, New Zealand: implications for the formation of epithermal vein deposits. *Econ. Geol.* **107**, 427–457. http://dx.doi.org/10.2113/econgeo.107.3.427.

Sánchez P., Pérez-Flores P., Arancibia G., Cembrano J. and Reich M. (2013) Crustal deformation effects on the chemical evolution of geothermal systems: the intra-arc Liquiñe-Ofqui fault system, Southern Andes. *Int. Geol. Rev.* **55**, 1384–1400. http://dx.doi.org/10.1080/00206814.2013.775731.

Sano Y. and Wakita H. (1988) Helium isotope ratio and heat discharge rate in the Hokkaido Island, Northeast Japan. *Geochem. J.* **22**, 293–303.

Sano Y. and Marty B. (1995) Origin of carbon in fumarolic gas from island arcs. *Chem. Geol.* **119**, 265–274.

Sano Y. and Williams S. N. (1996) Fluxes of mantle and subducted carbon along convergent plate boundaries. *Geophys. Res. Lett.* **23**, 2749–2752.

Sano Y., Nishio Y., Sasaki S., Gamo T. and Nagao K. (1998) Helium and carbon isotope systematics at Ontake volcano, Japan. *J. Geophys. Res.* **103**(B10), 23863–23873.

Sano Y., Takahata N., Nishio Y., Fischer T. P. and Williams S. N. (2001) Volcanic flux of nitrogen from the Earth. *Chem. Geol.* **171**, 263–271.

Sano Y., Takahata N. and Seno T. (2006) Geographical distribution of $^{3}He/^{4}He$ ratios in the Chugoku District, Southwestern Japan. *Pure Appl. Geophys.* **163**, 745–757.

Sano Y., Tokutake T. and Takahata N. (2008) Accurate measurement of atmospheric helium isotopes. *Anal. Sci.* **24**, 521–525.

Sano Y. and Fischer T. P. (2013) The analysis and Interpretation of Noble Gases in Modern Hydrothermal Systems. In *The Noble Gases as Geochemical Tracers. Advances in Isotope Geochemistry* (ed. P. Burnard). Springer-Verlag, pp. 249–317.

Sano Y., Marty B. and Burnard P. (2013) Noble gases in the atmosphere. In *The Noble Gases as Geochemical Tracers. Advances in Isotope Geochemistry* (ed. P. Burnard). Springer-Verlag, pp. 17–31.

Sepúlveda F., Dorsch K., Lahsen A., Bender S. and Palacios C. (2004) The chemical and isotopic composition of geothermal discharges from the Puyehue-CordónCaulle area (40.5°S), Southern Chile. *Geothermics* **33**, 655–673.

Sepúlveda F., Lahsen A. and Powell T. (2007) Gasgeochemistry of the CordónCaulle geothermal system, Southern Chile. *Geothermics* **36**, 389–420.

Sibson R. H. (1994) Crustal stress, faulting and fluid flow. In *Geological Society Special Publication*, Vol. 78 (ed. J. Parnell), pp. 69–84. http://dx.doi.org/10.1144/GSL.SP.1994.078.01.07.

Sibson R. H. (1996) Structural permeability of fluid-driven fault-fracture meshes. *J. Struct. Geol.* **18**, 1031–1042.

Sibson R. H. and Rowland J. V. (2003) Stress, fluid-pressure, and structural permeability in seismogenic crust, North Island, New Zealand. *Geophys. J. Int.* **154**, 584–594.

Somoza R. and Ghidella M. (2005) Convergencia en el margen occidental de América del Sur durante el Cenozoico: subducción de las placas de Nazca, Farallón y Aluk. *Rev. Asoc. Geol. Argent.* **60**(4), 797–809.

Stern C. R. (1991) Role of subduction erosion in the generation of the Andean magmas. *Geology* **19**, 78–81.

Stern C. R., Moreno H., López-Escobar L., Oliveros V., Clavero J. E., Lara L. E., Naranjo J. A., Parada M. A. and Skewes M. A. (2007) Chilean volcanoes. In *The Geology of Chile, 21–114* (eds. T. Moreno and W. Gibbons). The Geological Society, London, pp. 147–178.

Tassara A. and Yáñez G. (2003) Relación entre el espesor elástico de la litósfera y la segmentación tectónica del margen andino (15–47°S). *Rev. Geol. Chile* **30**, 159–186.

Tassara A., Gotze H. J., Schmidt S. and Hackney R. (2006) Three-dimensional density model of the Nazca plate and the Andean continental margin. *J. Geophys. Res.* **111**, b09404. http://dx.doi.org/10.1029/2005JB003976.

Varekamp J. C., DeMoor J. M., Merrill M. D., Colvin A. S. and Goss A. R. (2006) Geochemistry and isotopic characteristics of the Caviahue-Copahue volcanic complex, Province of neuquen, Argentina. *Geol. Soc. Am. Spec. Pap.* **407**, 317–342.

Vogel J. C., Grootes P. M. and Mook W. G. (1970) Isotopic fractionation between gaseous and dissolved carbon dioxide. *Z. Phys.* **230**, 255–258.

Associate editor: Jeffrey C. Alt